



**HAL**  
open science

## Active deformation in Ecuador enlightened by a new waveform-based catalog of earthquake focal mechanisms

Sandro Vaca, Martin Vallée, Jean-Mathieu Nocquet, Alexandra Alvarado

### ► To cite this version:

Sandro Vaca, Martin Vallée, Jean-Mathieu Nocquet, Alexandra Alvarado. Active deformation in Ecuador enlightened by a new waveform-based catalog of earthquake focal mechanisms. *Journal of South American Earth Sciences*, 2019, 93, pp.449 - 461. 10.1016/j.jsames.2019.05.017 . hal-03485889

**HAL Id: hal-03485889**

**<https://hal.science/hal-03485889>**

Submitted on 20 Dec 2021

**HAL** is a multi-disciplinary open access archive for the deposit and dissemination of scientific research documents, whether they are published or not. The documents may come from teaching and research institutions in France or abroad, or from public or private research centers.

L'archive ouverte pluridisciplinaire **HAL**, est destinée au dépôt et à la diffusion de documents scientifiques de niveau recherche, publiés ou non, émanant des établissements d'enseignement et de recherche français ou étrangers, des laboratoires publics ou privés.



Distributed under a Creative Commons Attribution - NonCommercial 4.0 International License

1           **Active deformation in Ecuador enlightened by a new**  
2                   **waveform-based catalog of earthquake focal**  
3                           **mechanisms**

4       Sandro Vaca<sup>a,b\*</sup>, Martin Vallée<sup>a</sup>, Jean-Mathieu Nocquet<sup>c,a</sup> and Alexandra Alvarado<sup>b</sup>

5           (a) Université de Paris, Institut de physique du globe de Paris, CNRS, F-75005  
6           Paris, France

7           (b) Instituto Geofísico-Escuela Politécnica Nacional, Quito, Ecuador

8           (c) Université Côte d'Azur, IRD, CNRS, Observatoire de la Côte d'Azur, Géoazur,  
9           Sophia Antipolis, France

10       \*Corresponding author: [svaca@igepn.edu.ec](mailto:svaca@igepn.edu.ec)

## 11 **Abstract**

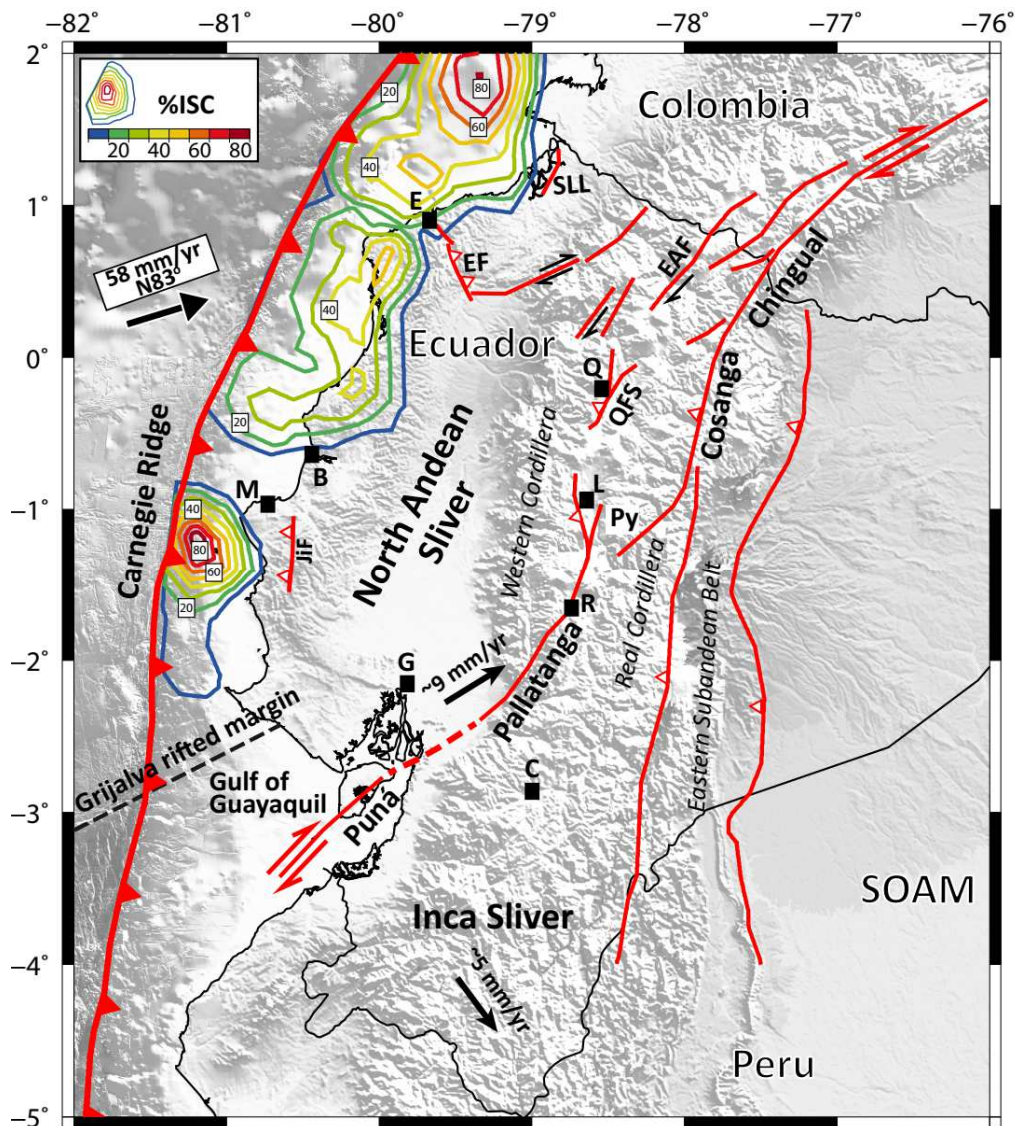
12           **The recent development of a national seismic broadband network in Ecuador**  
13 **enables us to determine a comprehensive catalog of earthquake focal mechanisms**  
14 **at the country-scale. Using a waveform inversion technique accounting for the**  
15 **spatially variable seismic velocity structure across the country, we provide location,**  
16 **depth, focal mechanism and seismic moment for 282 earthquakes during the 2009-**  
17 **2015 period. Our results are consistent with source parameter determinations at**  
18 **the global scale for the largest events, and increase the number of waveform-based**  
19 **focal mechanism solutions by a factor of two. Our new catalog provides additional**  
20 **constraints on the active deformation processes in Ecuador. Along the Ecuador**  
21 **margin, we find a correlation between the focal mechanisms and the strength of**  
22 **interseismic locking at the subduction interface derived from GPS measurements:**  
23 **thrust earthquakes predominate in Northern Ecuador where interseismic locking is**  
24 **high, while the low-to-moderate locking in Central and Southern Ecuador results in**  
25 **variable fault plane orientations. Focal mechanisms for crustal earthquakes are**  
26 **consistent with the principal axis of strain rate field derived from GPS data and with**  
27 **the location of the main active faults. Our catalog helps to determine the earthquake**  
28 **type to be expected in each of the seismic zones that have recently been proposed**  
29 **for probabilistic seismic hazard assessment.**

## 30 1. Introduction

31 The northern Andes is an area of complex tectonics due to the interaction of the  
32 Nazca, South America and Caribbean plates (Pennington, 1981; Kellogg and Bonini, 1982;  
33 Ego et al., 1996). The oblique convergence of the oceanic Nazca plate below the South  
34 America continent (Fig. 1) is partitioned between westward slip at the subduction  
35 interface and a northeastward escape of the North Andean Sliver (NAS) relative to South  
36 America (e.g., Pennington, 1981, Kellogg et al., 1985, Freymueller et al., 1993, Audemard &  
37 Audemard, 2002, Trenkamp et al., 2002, Nocquet et al., 2014, Mora-Paez et al., 2018, Fig.  
38 1). The NAS motion is predominantly accommodated by a large-scale regional dextral  
39 fault-system (Soulas et al., 1991), starting at the southern boundary of the Caribbean plate  
40 in Venezuela, running across Colombia along the foothills of the Eastern Cordillera (e.g.,  
41 Taboada et al., 1998), entering into Ecuador where it crosses the Andean cordillera, before  
42 finally reaching the gulf of Guayaquil (e.g., Audemard, 1993; Nocquet et al., 2014; Alvarado  
43 et al., 2016; Yepes et al., 2016; Fig. 1). In Ecuador, this major fault system has been named  
44 the Chingual-Cosanga-Pallatanga-Puná (CCPP) fault system, in reference to its individual  
45 segments (Alvarado et al., 2016). Secondary fault systems, with significant seismic hazard  
46 shown by large historical earthquakes (Beauval et al., 2010; Beauval et al., 2013), are also  
47 found west of this major fault system in the inter-andean valley, and east of it in the sub-  
48 andean domain (Alvarado et al., 2014; Alvarado et al., 2016; Yepes et al., 2016) (Fig. 1).

49 Along the Ecuadorian margin, elastic strain accumulation along the subduction is  
50 heterogeneous. In northern Ecuador, the high interseismic locking imaged by GPS (Fig. 1)  
51 is consistent with the large megathrust earthquakes observed during the XX<sup>th</sup> century  
52 [1906, Mw 8.4-8.8 (Kelleher, 1972; Kanamori and McNally, 1982; Ye et al., 2016;  
53 Yoshimoto et al., 2017); 1942, Mw 7.8 (Mendoza and Dewey, 1984); 1958, Mw 7.7

54 (Swenson and Beck, 1996); 1979, Mw 8.1 (Beck and Ruff, 1984); and the recent Mw 7.8  
 55 2016 Pedernales earthquake (Ye et al., 2016; Nocquet et al., 2017; Yoshimoto et al., 2017)].



57 **Fig. 1.** Tectonic map of Ecuador. The Nazca plate converges obliquely with respect to the stable  
 58 South American plate (SOAM) at 58 mm/yr (Kendrick et al., 2003), and relatively to the North  
 59 Andean Sliver (NAS) at 47mm/yr (Nocquet et al., 2014). The interseismic coupling (ISC) model  
 60 from Chlieh et al. (2014) is shown by the colored contours. With respect to Stable South America,  
 61 the NAS moves NNE-ward at ~9 mm/yr along the Chingual-Cosanga-Pallatanga-Puná (CCPP) fault  
 62 system (Nocquet et al., 2014; Alvarado et al., 2016). The Inca Sliver is moving toward the SSE at ~5  
 63 mm/yr (Nocquet et al., 2014; Villegas-Lanza et al., 2016), inducing shortening in the eastern sub-  
 64 Andean belt. The Grijalva fracture separates two domains of the Nazca plate with different ages and

65 densities (Lonsdale, 2005). Faults: SLL: San Lorenzo lineament; EF: Esmeraldas Fault; EAF: El Angel  
66 Fault; JiF: Jipijapa Fault; Py: Pisayambo zone; QFS: Quito active Fault System. Cities: E: Esmeraldas;  
67 B: Bahía; M: Manta; G: Guayaquil; Q: Quito; L: Latacunga; C: Cuenca; R: Riobamba.

68 Between latitudes 0.8S and 1.5S, the average coupling is low and only a small, shallow area  
69 close to La Plata island is found to be locked (Vallée et al., 2013; Chlieh et al., 2014; Collot  
70 et al., 2017). South of this area, the GPS data do not detect any significant coupling  
71 (Nocquet et al., 2014; Villegas-Lanza et al., 2016).

72         Aside from the large subduction earthquakes, destructive events mostly occurred  
73 along or close to the CCPP (Beauval et al., 2010; Beauval et al., 2013; Alvarado et al., 2016;  
74 Yepes et al., 2016). Large crustal events are expected to have long recurrence intervals  
75 (Baize et al., 2015), and as a consequence, historical events cannot fully characterize the  
76 type and locations of potential future earthquakes. An approach complementary to the  
77 historical earthquake catalog is to determine the rupture mechanism of small and  
78 moderate earthquakes. A preliminary attempt to characterize the seismogenic zones in  
79 Ecuador was made by Bonilla et al. (1992) who determined the spatial distribution of the  
80 active fault systems, using the earthquake depths and faulting styles provided by the focal  
81 mechanisms solutions. More recently, Yepes et al. (2016) proposed a new classification for  
82 the seismic source zones (SSZs) for subduction interface, intraslab and crustal events.  
83 Their classification takes into account focal mechanisms from the Global centroid moment  
84 tensor (GCMT) catalog (Dziewonski et al., 1981; Ekström et al., 2012), geological and  
85 geophysical information (tectonic and structural features of major faults, geodesy and  
86 paleoseismology). In total 19 SSZs have been characterized corresponding to the shallow  
87 subduction interface (3), intraslab (6), crustal (9), and outer rise (1) zones. Each of the SSZ  
88 is assumed to have a homogeneous seismogenic potential (Yepes et al., 2016). In this  
89 study, we use the zonation proposed by Yepes et al. (2016) and discuss its relations with  
90 our newly determined focal mechanism catalog.

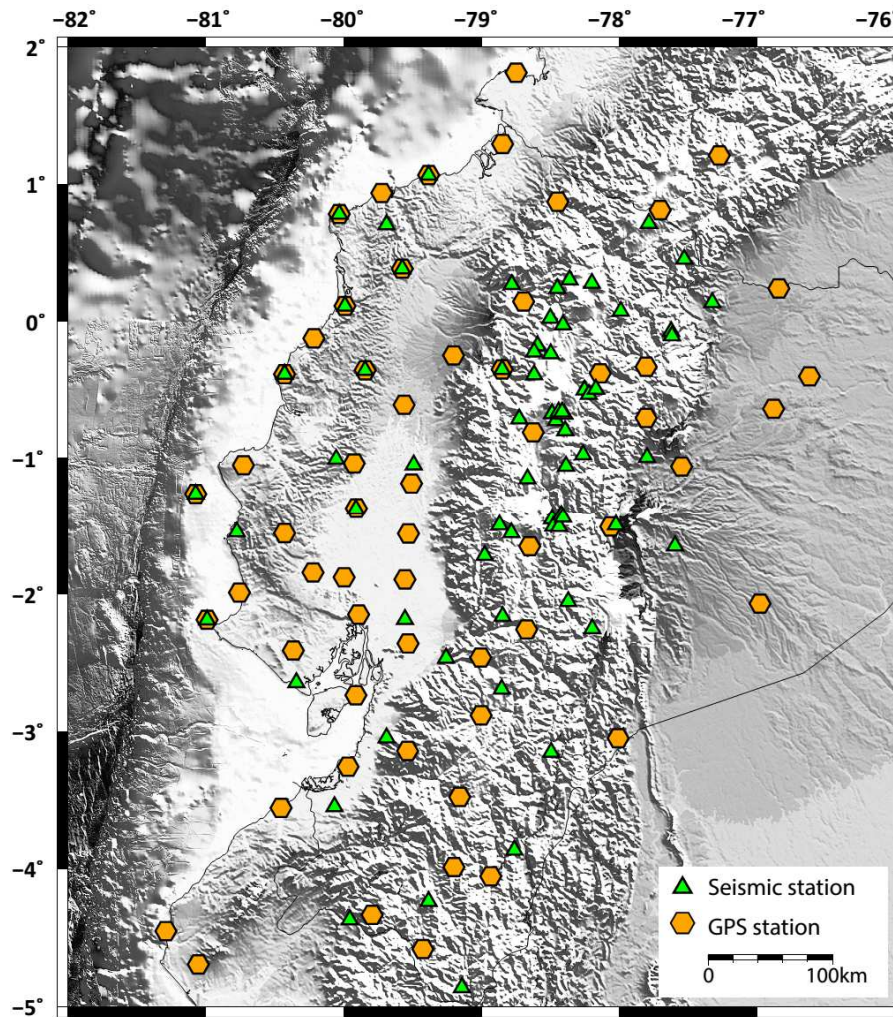
## 91 **2. Development of the broadband seismic network and new** 92 **potential for source parameters determination**

93 For the main part of the XX<sup>th</sup> century, Ecuador has been seismically instrumented  
94 only by sensors in the vicinity of its capital Quito. In 1904, the Astronomical Observatory  
95 installed there the first seismic instrument (Bosh-Omori), which was then replaced by a  
96 Mainka instrument in 1928. Later, a set of Sprengnether seismometers (two horizontal  
97 and one vertical components) was deployed in 1954. In 1963, the QUI station (composed  
98 of 3 high-gain and 3 long period instruments, both with horizontal and vertical  
99 components (López, 2005)) was installed in the western part of Quito in the framework of  
100 the World-Wide Standardized Seismographic Network (WWSSN). This station was moved  
101 in 1975 to South-west of Quito and was maintained until the 1980's by the "Instituto  
102 Geofísico de la Escuela Politécnica Nacional" (IG-EPN).

103 The local Ecuadorian seismic network started in the 1970's, with short period  
104 seismic stations mostly deployed temporarily in order to monitor volcanic activity and  
105 specific areas of the Inter-Andean-Valley (Yepes, 1982; Durand et al., 1987). The density of  
106 the stations in the Andes improved after the creation of the IG-EPN in 1983, and the  
107 seismic network was eventually extended to the coastal areas after 1991 (Vaca, 2006). In  
108 2002, the IRIS GSN station OTAV (close to Otavalo city) was the first permanent  
109 broadband station with real time transmission installed in the country. Since 2006, the  
110 seismic network has been regularly improved thanks to the efforts of IG-EPN together  
111 with the support of national government agencies (SENESCYT and SENPLADES), national  
112 and international partners (local governments, IRD, JICA, USAID, see Alvarado et al., 2018).  
113 The densification of the broad band network in the north-western zone of Ecuador started

114 at the end of 2008 with the ADN-project (Nocquet et al., 2010). Since 2011, a country-scale  
115 broadband network is progressively being installed, with the final objective to cover the  
116 most seismically active regions, from the coastal zone to the eastern foothills with an  
117 average ~50 km inter-station distance (Fig. 2).

118         Among other applications, the development of a country-wide broadband seismic  
119 network now allows us to determine the earthquake source parameters by waveform  
120 modeling. Since 2009, most of the events with moment magnitudes  $M_w > 3.5$  could be  
121 analyzed with the method described in the next section. Even with only a few years of  
122 data, a significant information increase is expected compared to the GCMT catalog, which  
123 has a magnitude threshold of about  $M_w 5.0$ . We also expect to improve the focal  
124 mechanism information previously provided by IG-EPN, which was based on first arrival  
125 polarities. Our final objective is to contribute to the “Ecuadorian focal mechanism catalog”,  
126 in which we will also provide more reliable information about source depths and moment  
127 magnitudes.

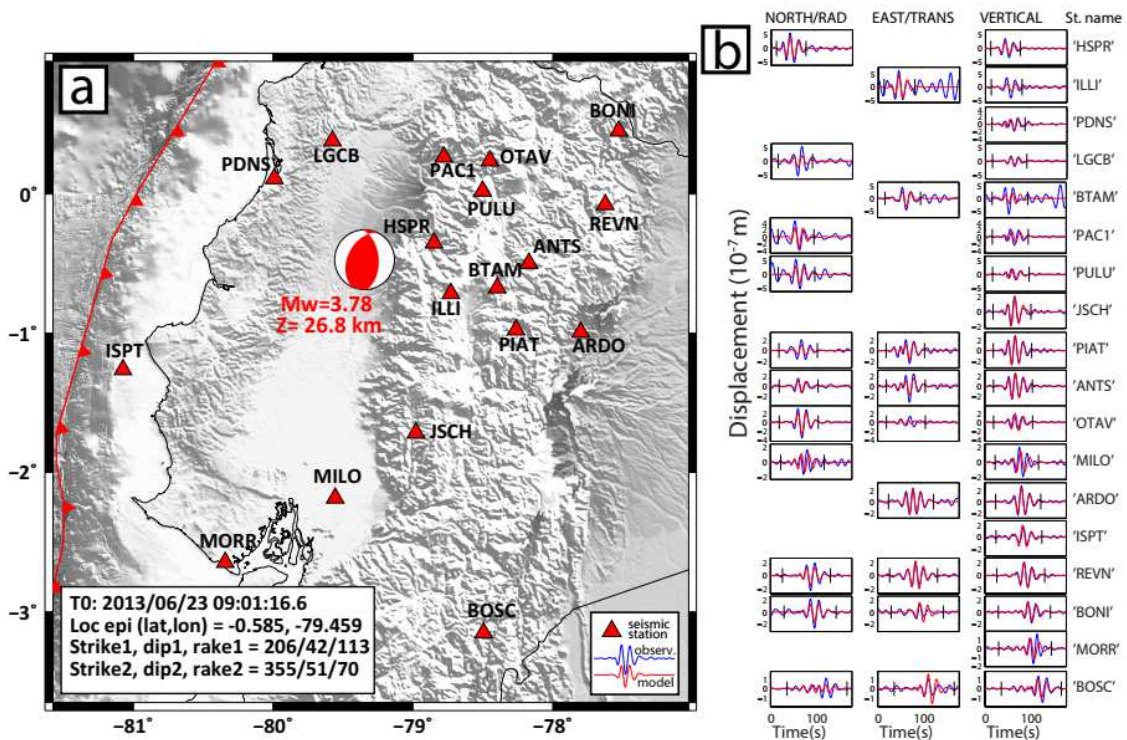


128 **Fig. 2.** Seismic (broadband, green triangles) and GPS networks (orange hexagons, Mothes et al.,  
 129 2013, 2018; Alvarado et al., 2018) in Ecuador as of December 2015. The dense arrays of seismic  
 130 stations in the central-northern part of the country are used for volcano monitoring. Additional GPS  
 131 stations in northern Peru and southern Colombia helping to define the regional kinematics are also  
 132 shown.

133 **3. Focal mechanism, depth and magnitude determination**

134           Several similar methods exist to analyze the broadband seismic waveforms in  
135 order to retrieve the source parameters [e.g. FMNEAR (Delouis, 2014); ISOLA (Zahradník  
136 et al., 2008)]. Here, we use the MECAVEL method, already used in several studies of  
137 moderate magnitude earthquakes (Mercier de Lepinay et al, 2011; Grandin et al., 2017). A  
138 specificity of the MECAVEL method is its ability to solve for the velocity model  
139 simultaneously with the searched source parameters (strike, dip, and rake of the focal  
140 mechanism, centroid location, source origin time and duration, and moment magnitude).  
141 The method starts from an initial solution (for origin time, hypocenter, and magnitude),  
142 here determined by IG-EPN. The velocity model is parametrized by a superficial low-  
143 velocity layer above a crustal structure with variable Moho depth. Crustal velocities are  
144 searched over a wide range, between 5.5km/s and 6.7km/s, and Moho depth can reach up  
145 to 67km. This approach is particularly useful when analyzing earthquakes occurring in  
146 different tectonic environments, as it is the case in Ecuador. Modeled waveforms in the  
147 tabular velocity model are computed using the discrete wave number method from  
148 Bouchon (1981), and the inverse problem is solved through the Neighborhood Algorithm  
149 (Sambridge, 1999). Within the MECAVEL method, the three-component displacement  
150 waveforms are bandpassed between a low frequency ( $F_{c1}$ ) and a high frequency ( $F_{c2}$ )  
151 threshold.  $F_{c1}$  is typically chosen above the low-frequency noise that may affect the  
152 waveforms for a moderate earthquake and  $F_{c2}$  is mostly controlled by the limited accuracy  
153 of the simplified one-dimensional structure model.  $F_{c2}$  must also not be chosen above the  
154 earthquake corner frequency, because the earthquake time history is simply modeled by a  
155 triangular source time function whose only inverted parameter is the global duration. In  
156 most of the cases analyzed here,  $F_{c1}$  on the order of 0.02-0.04Hz and  $F_{c2}$  on the order of  
157 0.05-0.07Hz are found to be suitable values. As a consequence, the source duration has a  
158 real role in the inversion procedure only for large events ( $M_w > 6.5$ ), for which it affects  
159 frequencies close to  $F_{c2}$ .

160 We extract all events reported with local magnitude larger than 3.8 from the  
 161 Ecuadorian national earthquake catalog (IG-EPN) for the period 2009-2015, and collect all  
 162 the available broadband seismic data in Ecuador. We then manually select the most  
 163 suitable waveforms, taking into account distance and azimuthal coverage and eliminating  
 164 components with a poor signal-to-noise ratio. For the 544 events with magnitude above  
 165 3.8, 326 were recorded with a quality sufficient for the waveform analysis.



166 **Fig. 3.** Example of a solution determined by the MECAVEL method. The map in (a) shows the  
 167 inverted source parameters (focal mechanism, moment magnitude  $M_w$  and depth  $Z$ ) and the  
 168 location of the broadband seismic stations used. The red line represents the trench. The left-bottom  
 169 inset provides the origin time ( $T_0$ ), the epicentral location and the angles (strike, dip, and rake) of  
 170 the conjugate nodal planes and rakes. The agreement between observed (blue) and synthetic (red)  
 171 waveforms is shown in b) for each station and component. The stations are sorted by increasing  
 172 epicentral distance from top to bottom. Here, data and synthetics are filtered between 0.04Hz and  
 173 0.06Hz. We excluded some components because of their poor signal-to-noise ratio in the selected  
 174 frequency range.

175           We use a criterion based on the misfit between data and synthetics, azimuthal  
176 coverage, and number of available stations and components, in order to ensure that only  
177 reliable solutions are kept. 44 events not meeting these criteria were rejected, resulting in  
178 a final catalog of 282 events. This catalog is provided as a public dataset linked to the  
179 present study (Vaca et al., 2019). Rejections are mostly related to earthquakes with low  
180 magnitudes located far away from the seismic network, and/or to earthquakes with an  
181 erroneous initial location preventing the MECAVEL method to converge. An example of  
182 focal mechanism determination for a Mw 3.8 earthquake is shown in Fig. 3.

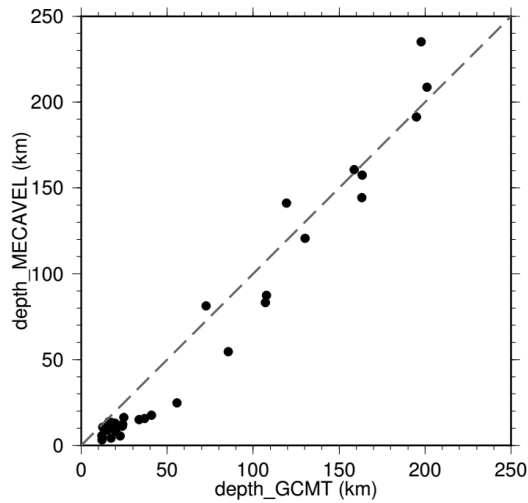
183           As a first validation of our method, we compared our results to the Global CMT  
184 solutions for the 34 events found in common during the 2009-2015 period. These  
185 earthquakes have a magnitude between Mw 4.8 and Mw 7.1 (Figs. 4 and 5). The focal  
186 mechanisms are very similar in almost all cases, even when compared to the full GCMT  
187 solution which includes the non-double-couple components. Only one event (2014/10/20,  
188 marked with a black asterisk in Fig. 4) located in the Andes close to the Ecuador-Colombia  
189 border, is significantly different. This event occurred during a seismic crisis related to a  
190 magmatic intrusion in the Chiles-Cerro Negro volcanic complex (IG-EPN, OSVP internal  
191 reports, Ebmeier et al., 2016). In such a context, a complex mechanism reflecting the  
192 superposition of volumetric changes and shear faulting (McNutt, 2005; Minson et al., 2007;  
193 Shuler and Ekström, 2009) would explain the strong non-double-couple component of the  
194 GCMT-solution and the difficulty to resolve this event with the double-couple MECAVEL  
195 method.

196           Compared with GCMT results, no general bias is observed for the full depth range,  
197 down to 200 km depth, and the average difference is 8 km (Fig. 5). This difference is due to  
198 the numerous events with depths shallower than 50km, for which GCMT determines  
199 deeper values than MECAVEL. This trend is likely due both to the minimum allowed depth

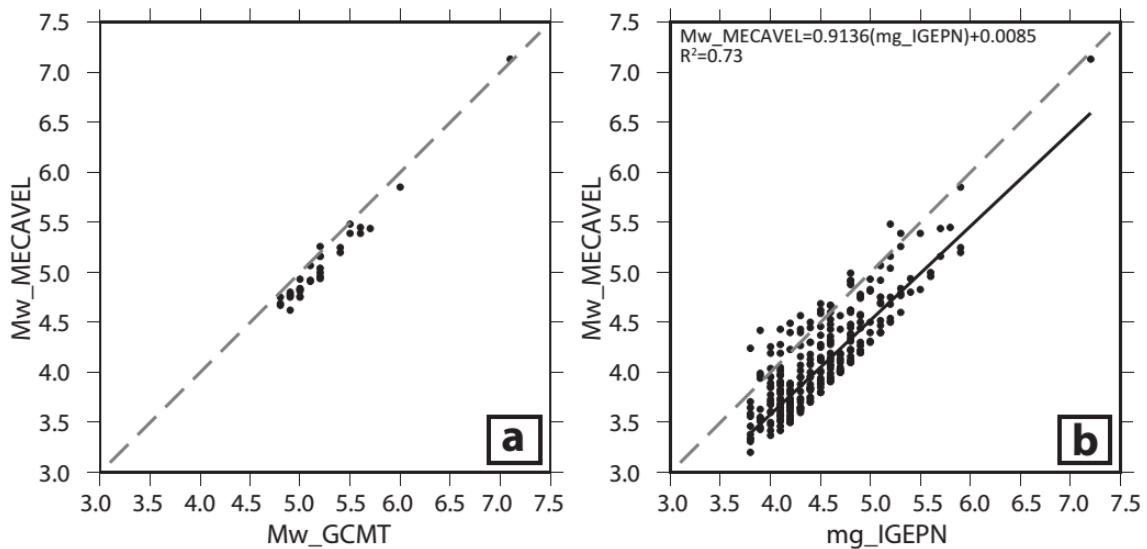
200 in the inversion (12km for GCMT and 3km for MECAVEL) and to slower velocity structures  
 201 found by MECAVEL. The comparison of magnitudes shows that those determined with the  
 202 MECAVEL method are slightly lower than the GCMT ones (average difference of 0.13, Fig.  
 203 6). On the contrary, magnitudes from IG-EPN catalog are systematically larger (average  
 204 difference of 0.38). Such observation should help to homogenize the magnitudes of the  
 205 local IG-EPN catalog, a step required to use a magnitude catalog for seismic hazard  
 206 estimation (e.g. Beauval et al., 2013).

	MECAVEL	GCMT		MECAVEL	GCMT
2009/02/21	 Z=16.3;Mw=4.83	 Z=24.8;Mw=5.0	2013/12/14	 Z=13.0;Mw=4.77	 Z=19.7;Mw=4.9
2009/05/01	 Z=191.4;Mw=5.07	 Z=194.9;Mw=5.1	2014/03/09	 Z=11.9;Mw=5.39	 Z=15.0;Mw=5.6
2009/10/09	 Z=13.3;Mw=5.16	 Z=17.5;Mw=5.2	2014/03/25	 Z=5.6;Mw=5.00	 Z=12.0;Mw=5.2
2010/02/28	 Z=15.0;Mw=5.04	 Z=33.7;Mw=5.2	2014/04/30	 Z=8.9;Mw=4.78	 Z=15.0;Mw=4.9
2010/03/26	 Z=3.1;Mw=4.76	 Z=12.0;Mw=5.0	2014/06/16	 Z=13.7;Mw=5.44	 Z=16.0;Mw=5.7
2010/08/12	 Z=235.1;Mw=7.13	 Z=197.8;Mw=7.1	2014/08/12	 Z=10.5;Mw=4.92	 Z=12.5;Mw=5.1
2010/10/09	 Z=141.1;Mw=5.26	 Z=119.4;Mw=5.2	2014/08/16	 Z=8.9;Mw=4.62	 Z=19.8;Mw=4.9
2011/05/12	 Z=5.4;Mw=4.83	 Z=22.7;Mw=5.0	2014/10/20	*  Z=5.8;Mw=5.45	*  Z=12.0;Mw=5.6
2011/07/26	 Z=120.6;Mw=4.93	 Z=130.2;Mw=5.0	2014/11/11	 Z=144.3;Mw=4.67	 Z=163.2;Mw=4.8
2011/11/17	 Z=10.4;Mw=5.85	 Z=15.5;Mw=6.0	2014/12/03	 Z=157.4;Mw=4.94	 Z=163.4;Mw=5.2
2012/01/10	 Z=15.7;Mw=4.91	 Z=36.8;Mw=5.1	2014/12/21	 Z=8.3;Mw=4.81	 Z=20.0;Mw=5.0
2012/01/19	 Z=4.3;Mw=4.75	 Z=17.4;Mw=4.9	2015/01/16	 Z=54.7;Mw=4.96	 Z=85.6;Mw=5.2
2012/02/08	 Z=24.8;Mw=5.16	 Z=55.6;Mw=5.2	2015/03/19	 Z=17.5;Mw=4.80	 Z=40.8;Mw=4.9
2012/05/23	 Z=160.7;Mw=4.69	 Z=158.8;Mw=4.8	2015/03/27	 Z=208.8;Mw=5.48	 Z=201.0;Mw=5.5
2012/06/08	 Z=11.9;Mw=4.75	 Z=18.4;Mw=5.0	2015/04/28	 Z=83.2;Mw=5.20	 Z=107.2;Mw=5.4
2012/07/30	 Z=12.2;Mw=4.84	 Z=24.1;Mw=5.0	2015/05/30	 Z=11.2;Mw=5.25	 Z=24.0;Mw=5.4
2013/04/29	 Z=81.2;Mw=4.75	 Z=72.5;Mw=4.8	2015/10/15	 Z=87.5;Mw=5.39	 Z=107.8;Mw=5.5

207 **Fig. 4.** Comparison between MECAVEL (double couple) with GCMT solutions (full solution) for the  
 208 common events of the 2009-2015 period. The date of the earthquake occurrence is shown to the  
 209 left of the focal mechanisms. Depths (Z) and magnitudes (Mw) are shown to the right of the focal  
 210 mechanisms.

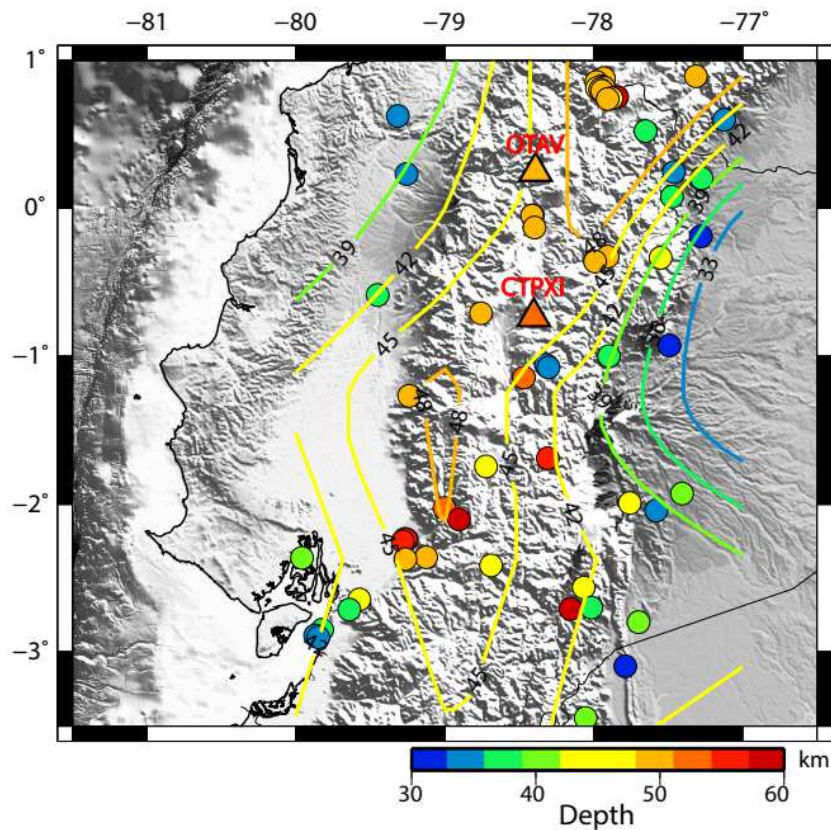


211 **Fig. 5.** Depth comparison for the events common to GCMT and MECVEL (this study). Dashed lines  
 212 show the line along which the considered depths are equal.



213 **Fig. 6.** Magnitude comparison for the events common to GCMT, MECVEL (this study) and IG-EPN  
 214 local catalog. a) Comparison between GCMT and MECVEL b) Comparison between MECVEL and  
 215 IG-EPN. The equation of the linear regression between the two magnitude catalogs (and the  
 216 associated correlation coefficient  $R^2$ ) is shown in the figure. This equation can be used to convert  
 217 the local magnitudes to moment magnitudes in order to homogenize the local catalog. In a) and b)  
 218 the dashed lines show the line along which the considered magnitudes are equal. “mg\_IGEPN”  
 219 refers to the preferred magnitude reported by IG-EPN.

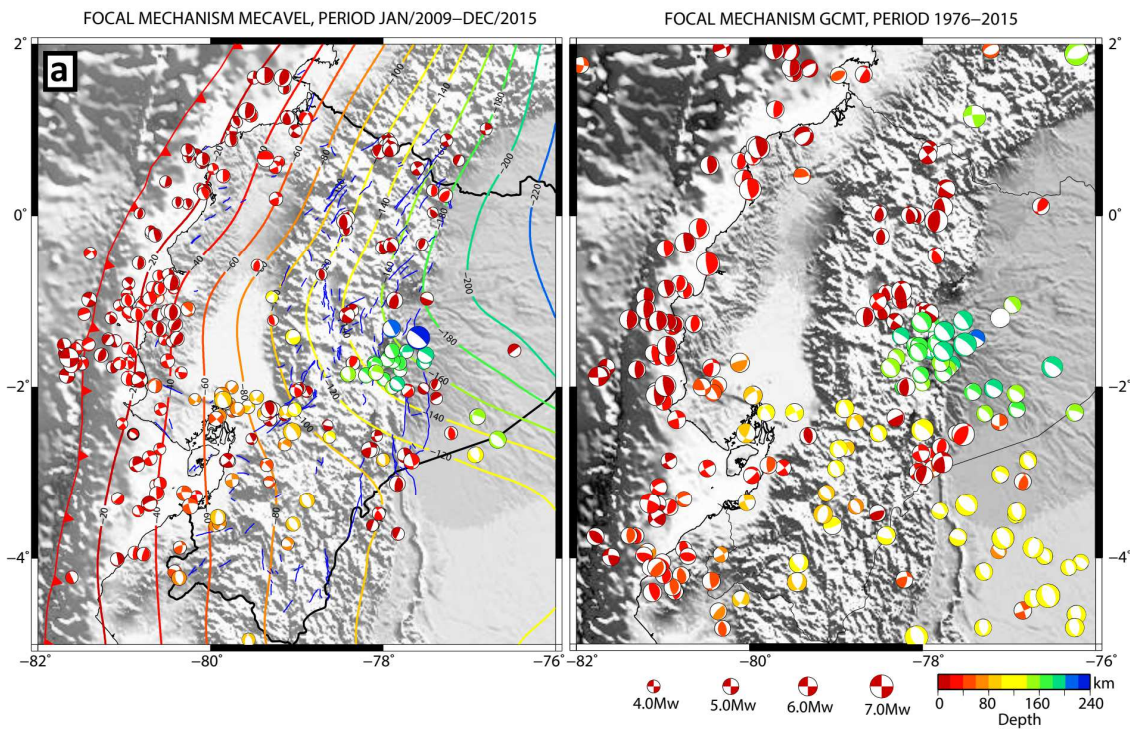
220           As another validation of the MECAVEL method, we show in Fig. 7 that the  
221 optimized 1D model is consistent with the large-scale features of the crustal thickness in  
222 Ecuador. In particular, the Moho depth approaches 50 km beneath the ~150 km-wide  
223 Andes mountain range (Robalino, 1977; Chambat, 1996); and as expected, the crustal  
224 thickness is thinner when entering into the subandean area or into the coastal domain.  
225 Crustal thicknesses obtained from Receiver Functions show Moho depths of ~53 km  
226 under the Cotopaxi volcano in the central Andes (Bishop et al., 2017), and of ~50 km  
227 below OTAV station (Poveda et al., 2015). We show in Fig. 7 that the latter values are  
228 consistent with the neighboring Moho depths inferred from MECAVEL. Crustal depths  
229 determined in the subduction area (not shown in Fig. 7) are less consistent from one  
230 earthquake to the other, which can be simply understood by the fact that the one-  
231 dimensional parametrization is too simplistic in a subduction context. This generally  
232 illustrates that in a structurally complex area, the velocity structure determined by the  
233 MECAVEL method has to be considered as an equivalent model, possibly not directly  
234 related to the actual structure.



235 **Fig. 7.** Moho depths inferred from the MECAVEL inversion results. The depth contours are  
 236 interpolated from the Moho depths individually determined for each earthquake (colored points).  
 237 The subduction area is not considered here, as the tabular model is not expected to provide  
 238 meaningful information in a context of 2D/3D structure complexities. Colored triangles show Moho  
 239 depths obtained from Receiver Functions at the two following locations: CTPXI (Cotopaxi Volcano)  
 240 and OTAV (IRIS GSN station close to Otavalo).

241 In Fig. 8, we finally show the 210 solutions reported by GCMT (Ekström et al.,  
 242 2012) for the 1976-2015 period together with the 282 solutions determined here in the  
 243 2009-2015 period. We observe a general consistency of the focal mechanisms between the  
 244 two catalogs, in all of the seismically active areas of the country. The two catalogs  
 245 complement each other, with areas where information about the earthquake mechanism  
 246 type is richer in the MECAVEL or, on the contrary, in the GCMT catalog. In the next section,  
 247 we discuss the combined catalog in the light of the active deformation processes in

248 Ecuador. This combined catalog uses the MECAVEL solution for the events common with  
249 GCMT, but as shown by the similarities of the 34 common solutions in Figure 4, this choice  
250 does not influence any further interpretation of the focal mechanisms.



251 **Fig. 8.** Focal mechanisms provided (a) by the MECAVEL method (this study, 2009-2015) and (b) by  
252 the GCMT double-couple solutions (1976-2015). In a) and b) the earthquake depths and the iso-  
253 depths (in km) contours of the slab (Hayes et al., 2012) are color-coded with the same color scale  
254 (shown at the bottom right). The thick red line with triangles represents the trench.

#### 255 **4. Focal mechanisms and deformation processes in Ecuador**

256 For the sake of clarity, we separate the focal mechanism (FMs) according to their  
257 depths and their locations along the margin or in the continental domain. Figs. 9 and 10

258 show events shallower than 35 km (used to analyze the partitioning features in Fig. 11),  
259 and Fig. 12 shows the events deeper than 35 km. Although this division is somehow  
260 arbitrary, it is convenient to first discuss the state of stress at the subduction interface and  
261 within the overriding plate. Within the continental domain, it allows to separate the events  
262 related to crustal tectonics from deep slab-related events.

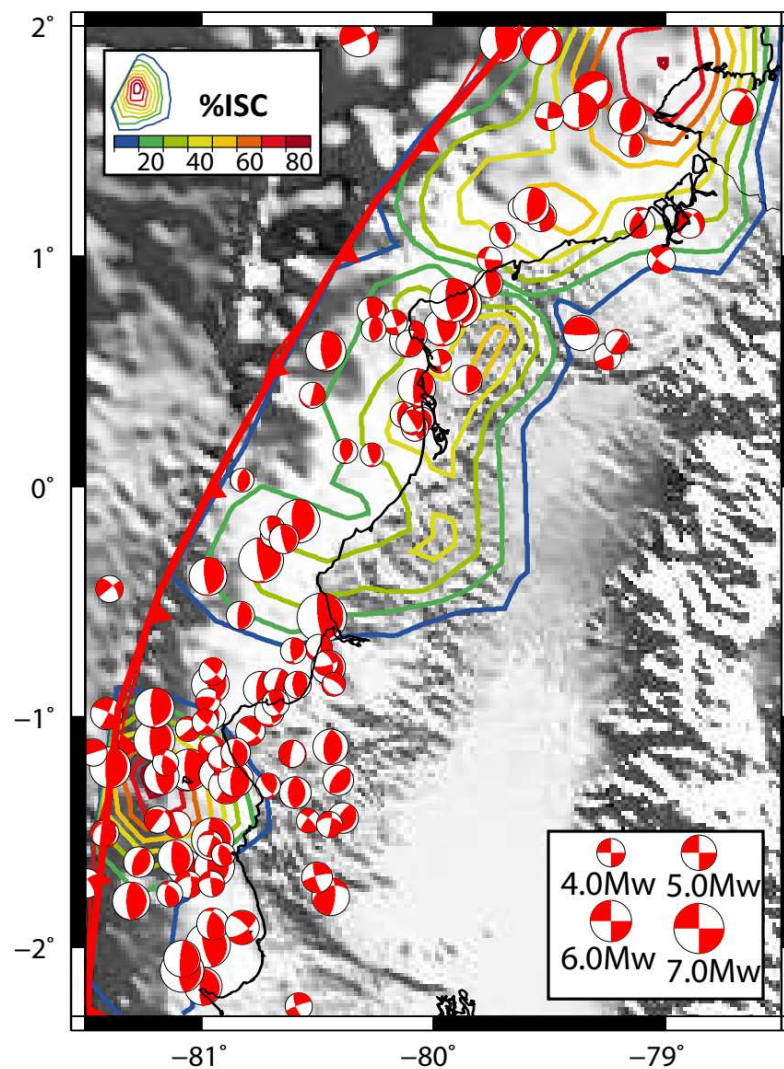
## 263 **4.1. Subduction**

264 Overall, the location of the earthquakes studied here is in agreement with the  
265 study from Font et al. (2013), who found that earthquakes during the interseismic period  
266 are spatially organized into several stripes of seismicity, most of them being perpendicular  
267 to the trench (Fig. 9).

### ***4.1.1. Northern Ecuador***

268 This zone hosted a large megathrust earthquakes sequence during the XX<sup>th</sup> century  
269 with magnitudes Mw 7.7-8.8 (Kelleher, 1972; Beck and Ruff, 1984; Mendoza and Dewey,  
270 1984; Swenson and Beck, 1996). In our catalog, this area is characterized by thrust events  
271 at or close to the subduction interface (Fig. 9). An interesting spatial correlation shows up  
272 with the interseismic locking models. Indeed, from latitude 0.8°N and further north, high  
273 locking is found from the trench to a depth of ~30 km. Location of the focal mechanisms  
274 determined here appears to outline the area of high locking, with only very few events  
275 located within areas of locking higher than 60% (Fig. 9). Focal mechanisms rather  
276 correlate with areas of the largest interseismic locking gradients, either downdip or  
277 laterally. This observation is for instance similar to the Himalaya where the small

278 seismicity appears to delimit the downdip limit of locking, where shear stress at the  
279 interface is the largest during the interseismic period (Avouac [et al.](#), 2015). This seismicity  
280 also appears to occur during seismic swarms related to slow slip events as found by Vaca  
281 [et al.](#) (2018) for the Punta-Galera Mompiche zone area located around lat. 0.8°N. The  
282 thrust mechanisms found in this study are compatible with this interpretation, although a  
283 few shallow strike-slip mechanisms reflect additional deformation within the overriding  
284 plate along the San Lorenzo lineament and the Esmeraldas fault (Fig. 1).



285 **Fig. 9.** Combined GCMT and MECAVEL (1976-2015) shallow FMs solutions (depth shallower than  
286 35 km) for the central and northern Ecuador margin. The interseismic locking model from Chlieh et  
287 al. (2014) is shown by the colored contours. The thick red line with triangles represents the trench.

#### 4.1.2. The Pedernales segment

288 The Pedernales segment, between lat. 0.7°N and 0.5°S, possibly ruptured during  
289 the 1906 earthquake, and hosted the 1942 Mw 7.8-7.9 and the recent 2016 Pedernales Mw  
290 7.8 earthquakes (Swenson and Beck, 1996; Ye et al., 2016; Nocquet et al., 2017). Along this  
291 segment, interseismic locking is confined between 10 and 30 km depth, in agreement with  
292 the location of the 2016 Pedernales earthquake, whose main rupture propagated below  
293 the coast between latitudes 0.4°N and 0.4°S (Nocquet et al., 2017). Our catalog, which ends  
294 in 2015, exhibits interesting spatial relationships with the rupture areas of the  
295 forthcoming Pedernales earthquake. First, our catalog shows that very few earthquakes  
296 occurred within the area of large (>1 m) co-seismic slip of the Pedernales earthquake (Fig.  
297 9 and Nocquet et al., 2017) during the years before the event. Secondly, at lat. ~0.2°S, our  
298 catalog highlights a larger density of events. That area did not rupture during the 2016  
299 earthquake but experienced large and rapid localized afterslip immediately after  
300 (Rolandone et al., 2018). It also hosted regular seismic swarms (Segovia, 2016) and  
301 repeating earthquakes during the years before the Pedernales earthquakes, although no  
302 associated slow slip event here has been geodetically found yet (Rolandone et al., 2018).  
303 The focal mechanisms found in this study are also predominantly thrust, consistent with  
304 slip at the interface (Figs. 9, 10). In this area, deformation therefore does not appear to be

305 accommodated by infrequent large earthquakes, but rather by numerous moderate  
306 earthquakes, seismic swarms (possibly associated with aseismic slip) and afterslip.

#### *4.1.3. The Bahía de Caráquez and La Plata Island segments*

307 The Bahía area (Figs. 9, 10), between latitudes 0.5°S and 1°S, experienced three M  
308 ~7 earthquakes in 1896, 1956 and 1998 (Mw 7.1) (Segovia et al., 1999; Yepes et al., 2016).  
309 In that area, our study shows mostly thrust mechanisms, compatible with interface  
310 subduction earthquakes. Although Yepes et al. (2016) consider the Pedernales and Bahía  
311 asperities to behave independently one from each other, the seismicity distribution does  
312 not show clear patterns to support this view. The Bahía and Pedernales segments are now  
313 considered as the same seismic zone (Beauval et al., 2018).

314 Between latitudes 1°S and 1.5°S, the central margin in Ecuador includes a 50 x 50  
315 km<sup>2</sup> area of high ISC (Figs. 1 and 9), around the “La Plata Island”, found to correlate with  
316 the presence of a subducted oceanic relief (Collot et al., 2017). This zone marks a  
317 transition between the mostly locked areas to the north and the southern Talara zone (Fig.  
318 10) which shows weak to negligible interplate locking. Episodic slow slip events,  
319 associated with seismic swarms seem to release part of the slip deficit there (Vaca et al.,  
320 2009; Font et al., 2013; Vallée et al., 2013; Chlieh et al, 2014; Jarrin, 2015; Segovia et al.,  
321 2018). In the central margin, the mechanisms of the abundant seismicity are more diverse  
322 than in Northern Ecuador (Figs. 9, 10), varying from reverse to strike-slip. The presence of  
323 Carnegie ridge may be an element explaining this variability, perhaps through the  
324 influence of various seamounts locally perturbing the stress field (Collot et al., 2017).  
325 Alternatively, strike-slip events might be located within the slab, indicating internal  
326 deformation of the subducting Carnegie ridge.

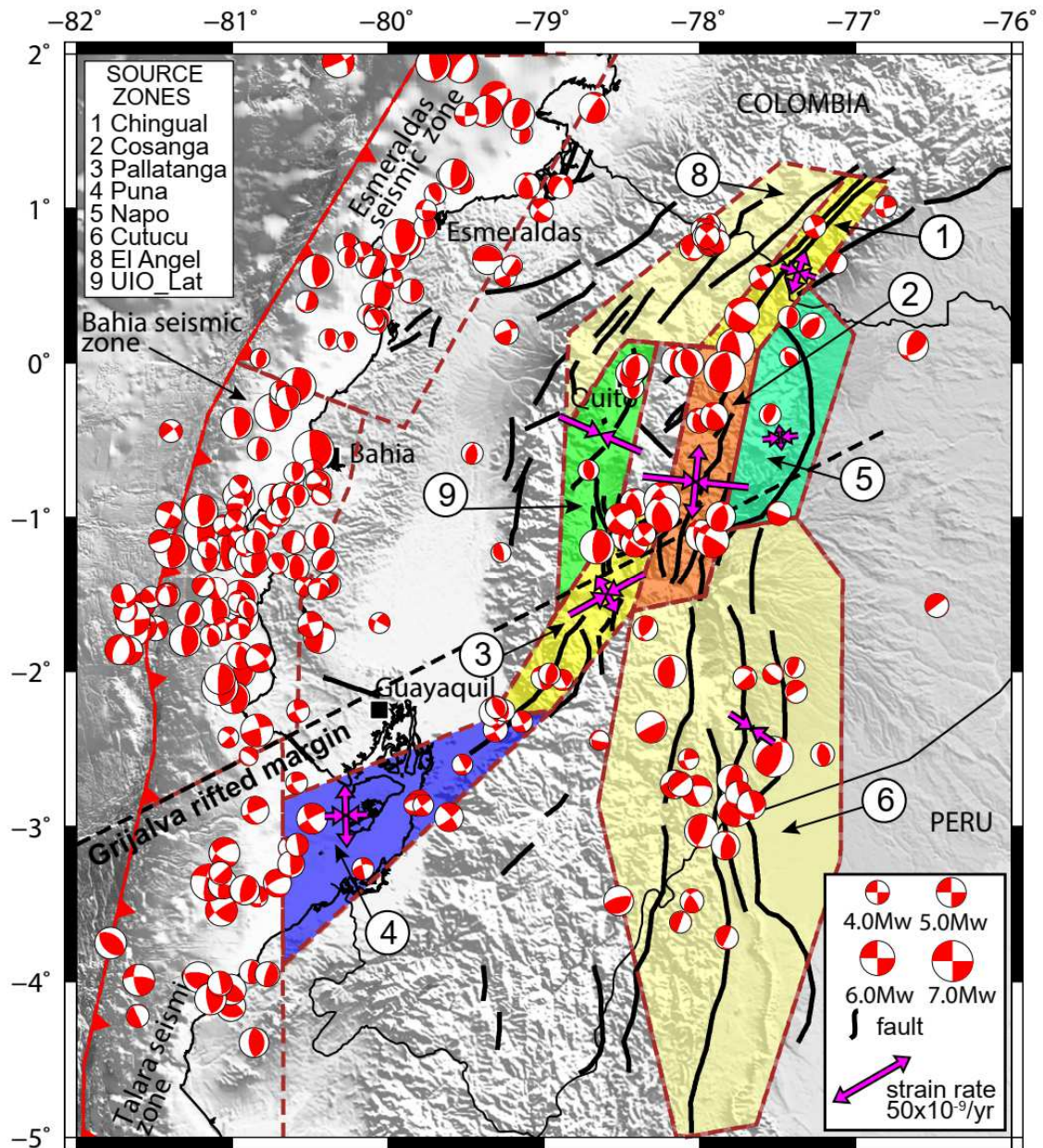
327           This area also shows outer-rise seismicity occurring within the Nazca plate, west of  
328 the trench, in the Carnegie ridge domain (Figs. 9, 10). Part of the seismicity might be  
329 related to the slab flexure (Collot et al., 2009), which is evidenced here by the presence of  
330 a few normal mechanisms. Nevertheless, most of the earthquakes show strike-slip  
331 mechanisms with planes azimuths ranging from N-S to NE-SW, like the one of 2011/11/17  
332 (Mw 5.9 MECAVEL, Mw 6.0 GCMT; Figs. 4, 8, 9 and 10). Such kind of seismicity could be  
333 related to two aligned ridges of ~W-E **direction** (with a 30km separation) and to some  
334 structures of the Nazca Plate aligned N55°E, observed in the bathymetry (Michaud et al.,  
335 2006; Collot et al., 2009). Because of the recurrent seismicity and the reported  
336 magnitudes, we suggest that the outer-rise Carnegie ridge could be added as an additional  
337 seismic zone for future PSHA models.

338           Further inland, an aligned N-S cluster with mostly reverse FMs is observed  
339 between lat. 1.8°S and 1.2°S. Béthoux et al. (2011), observing a similar pattern of focal  
340 mechanisms, suggest that some of them are not related to the interface but to the N-S  
341 oriented Jipijapa fault (Fig. 1) (Egüez et al., 2003), especially those showing steep dips  
342 (~30°) and shallow hypocenters (less than 20 km depth).

#### ***4.1.4. Southern Ecuador and northern Peru***

343           South of the Grijalva fracture (Fig. 10), very few thrust events are observed. This  
344 can be related to the very low subduction interface locking in this area (Nocquet et al.,  
345 2014; Villegas-Lanza et al., 2016). The faulting mechanisms are dominantly strike-slip  
346 with a few normal events (Fig. 10), in agreement with the NNE-SSW opening of the Gulf of  
347 Guayaquil (Deniaud et al., 1999; Calahorrano, 2005; Witt et al., 2006) and the relative  
348 motion between the NAS and the Inca Sliver (Nocquet et al., 2014).

349            Interestingly, we observe a general correlation between the level of locking and the  
350 diversity of focal mechanisms. For the locked Northern segments (see Fig. 1), thrust  
351 mechanisms consistent with the Nazca-NAS convergence dominate, suggesting that  
352 locking at the plate interface controls the stress field both at the plate interface and within  
353 the overriding margin. Oppositely, south of La Plata Island ( $\sim 1.5^\circ\text{S}$ ) where locking is weak  
354 or confined to the shallowest part of the subduction interface, thrust mechanisms show  
355 variable orientations of shortening. Additionally, normal and strike-slip mechanisms,  
356 consistent with known crustal faults (e.g. Bethoux et al., 2011) are frequent. Thus, the  
357 heterogeneous stress field along that segment therefore appears to result from a  
358 combination of crustal stress associated with slow straining of the overriding plate and  
359 reduced compressional stress in the plate convergence direction.

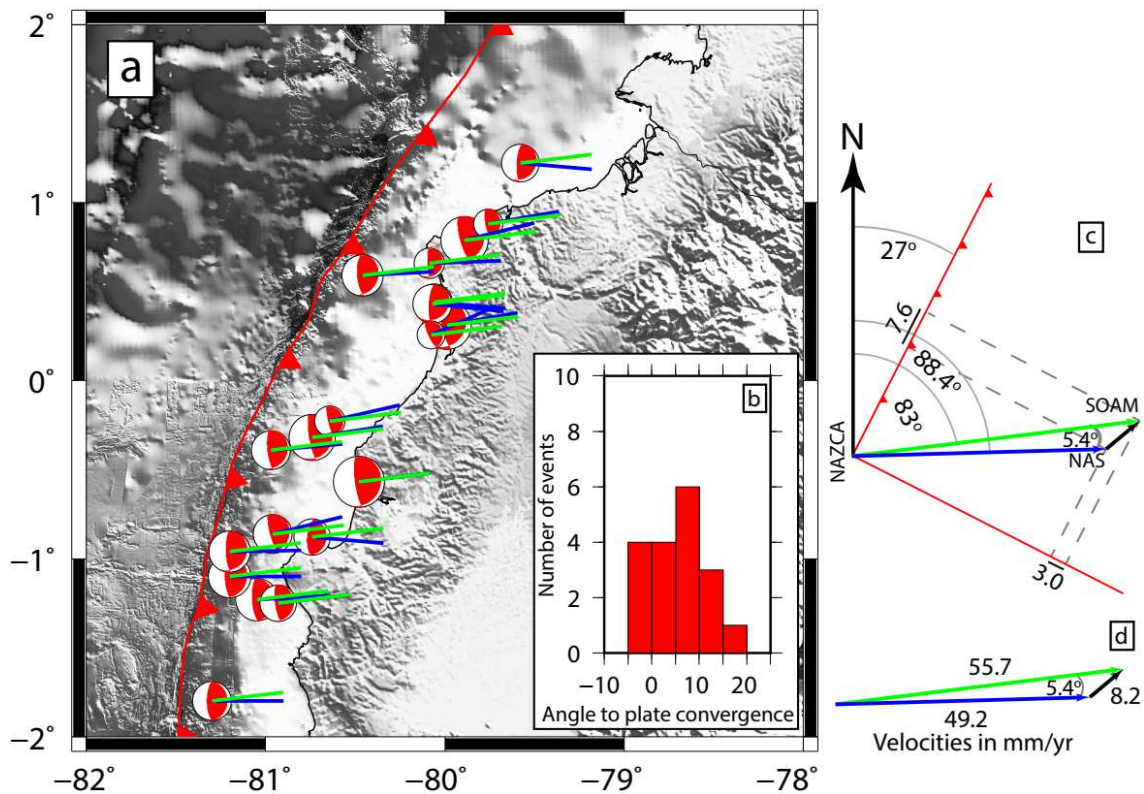


360 **Fig. 10.** Joint CGMT and MECAVEL shallow FM solutions (depth shallower than 35 km). We keep  
 361 the conventions chosen by Yepes et al. (2016) for interface (non-colored polygons) and upper-  
 362 crustal (colored polygons) seismic source zones (SSZs). Faults distribution is modified from  
 363 Alvarado et al. (2016). The strain rate axes are calculated from GPS velocities measured within or  
 364 close from each SSZ (see Fig. S1 and Table S1). We exclude the strain tensor of El Angel SSZ, because  
 365 **too few velocities are** available there. The red line represents the trench.

#### 4.1.5 Strain partitioning in the Ecuadorian subduction regime

366 In subduction contexts with oblique convergence, the motion obliquity is generally  
367 not fully accommodated by slip at the plate interface (e.g. McCaffrey, 1992). In this case, a  
368 forearc sliver is expected to move in a direction parallel to the trench, resulting in strike-  
369 slip faulting along one or several faults within the overriding plate (e.g., Chemenda et al.,  
370 2000). In addition, the trench perpendicular component of plate convergence may also be  
371 partitioned between slip at the subduction interface and thrust in the back-arc domain.

372 We examine here how focal mechanisms observed in Ecuador help to constrain the  
373 degree of partitioning. To do so, we first compute the angle difference between the  
374 surface-projected slip vector of interplate earthquakes and the Nazca/South America  
375 convergence direction. This approach neglects the small 3D component of the slip vector,  
376 and relies on the assumption that motion at the subduction interface is fully characterized  
377 by earthquakes (even if it can also be accommodated by aseismic processes). We select the  
378 FMs (GCMT and MECAVEL) of events located at the margin with hypocentral depths less  
379 than 35 km, nodal planes with strikes between  $0^\circ$  to  $45^\circ$ , dip shallower than  $25^\circ$ , and rakes  
380 between  $90^\circ$  and  $150^\circ$ , as these events are expected to have sources along the interface  
381 (Fig. 11a). After averaging over the earthquakes (Fig. 11 b), the angle difference between  
382 the slip vector and the Nazca/South America convergence direction is found equal to  $5.4^\circ$   
383 ( $\pm 6.2^\circ$ ), clockwise with respect to the Nazca/SOAM convergence (Fig. 11c and 11d).  
384 Although marginally significant, the average direction of subduction slip vector suggests  
385 that the subduction obliquity is not fully accommodated by slip at the subduction  
386 interface. Its value is further consistent with the escape of the NAS with respect to SOAM.



387 **Fig. 11.** Partitioning evidenced from FMs (GCMT and MECAVEL) subduction interface events. (a)  
 388 The surface-projected slip vector of each focal mechanism is shown by blue lines, together with the  
 389 Nazca/SOAM convergence direction (green lines). (b) The histogram shows the angle (in degrees)  
 390 between Nazca/SOAM **convergence direction and slip vector direction**, by bins of 5 degrees. Values  
 391 range between -5° and 15°, resulting in an average and standard error of 5.4° and 6.2°, respectively.  
 392 (c) Construction of the kinematic triangle. Average azimuth of the trench and its normal (red lines),  
 393 Nazca/SOAM convergence direction and amplitude (green vector), and the mean slip direction  
 394 deduced from FMs (blue) are first reported. The additional information on the NAS/SOAM relative  
 395 direction (black arrow, ~50° azimuth), constrained by the purely strike-slip motion observed in the  
 396 Chingual area (zone 1 in Figure 10), allows us to determine the kinematic triangle. This kinematic  
 397 triangle is shown in (d) with the assumed velocity of Nazca/SOAM (green), and the computed  
 398 velocities of Nazca/NAS (blue) and NAS/SOAM (black).

399 To further quantify the amount of partitioning, we use the seismicity observed in  
 400 the Chingual area (zone 1 in Figure 10), where most of the FMs are purely strike-slip with

401 one of their nodal planes directed along a  $\sim 50^\circ$  azimuth. Using this additional information  
402 together with the amplitude of the Nazca/SOAM convergence (55.7 mm/yr as reported at  
403  $0^\circ\text{N}$  by Kendrick et al. (2003)) allows us to determine the kinematic triangle (Fig. 11c and  
404 11d). The relative motion Nazca/NAS is found equal to 49.2 mm/yr, to be compared with  
405 the value of 47.5mm found by Nocquet et al. (2014). The relative motion NAS/SOAM is  
406 found equal to 8.2mm/y, in agreement with the geological slip rates of  $7.3 \pm 2.7$  mm/yr  
407 (Ego et al., 1996; Tibaldi et al., 2007) and the values between 7.5 and 9.5 mm/yr derived  
408 from GPS data (Nocquet et al., 2014). If using an average azimuth of  $27^\circ$  for the trench in  
409 Northern Ecuador, the ratio of partitioning is about 25% for the along-trench component  
410 of the Nazca/South America convergence (Fig. 11c). Normal trench convergence is also  
411 partitioned with 6% of the convergence being transferred to the motion of the NAS.

## 412 **4.2. Crustal deformation**

413 Using the selection of focal mechanisms shown in Fig. 10, we compare the style of  
414 faulting with recent kinematic models for inland Ecuador (Alvarado et al., 2016) and the  
415 seismic zonation proposed by Yepes et al. (2016). We further compare the principal axes  
416 of the horizontal strain rate tensor against the focal mechanisms. The strain rate tensors  
417 provided in Table S1 (Supplemental Information) are derived from the GPS velocities  
418 shown in Fig. S1, using least-squares and estimating a constant velocity gradient (Aktug et  
419 al., 2009) within the individual areas shown in Fig. 10.

#### 4.2.1. The Chingual-Cosanga-Pallatanga-Puná Fault System (CCPP)

421           The CCPP is the main fault system accommodating the 7.5 – 9.5 mm/yr motion of  
422 the NAS with respect to the stable part of the South America plate (Nocquet et al., 2014,  
423 Alvarado et al., 2016). Variation in strike, slip rate and faulting styles have been used to  
424 define separated segments for the seismic zonation presented in Yepes et al. (2016).

425           The Chingual seismic zone is the northern segment of CCPP (Fig. 1, marked as zone  
426 1 in Fig. 10), crossing the border with Colombia. It delimits the boundary between the NAS  
427 and the Amazon basin, which is assumed to be part of the stable part of the South America  
428 plate, as indicated by small GPS velocity residuals (<2 mm/yr) east of the Andes. As a  
429 consequence, the motion is expected to be mostly right-lateral strike-slip (Ego et al., 1995;  
430 Tibaldi et al., 2007). Little seismicity is observed along this segment. The two focal  
431 mechanism solutions (see zone 1 in Fig. 10) are consistent with dextral strike-slip on the  
432 NE-oriented planes. Nonetheless, the faults located at the feet of the eastern Andes  
433 indicate shallow dipping thrust. The strain rate tensor derived from GPS is in good  
434 agreement with right-lateral shear along N30° trending faults.

435           South of the Chingual segment, the Cosanga fault system (zone 2, Fig. 10) delimits  
436 the boundary between the NAS and the Sub-andean domain. Focal mechanisms show  
437 reverse slip with a slight right-lateral strike-slip component along the NS nodal plane. This  
438 seismic source is described as a transpressive zone (Ego et al., 1996; Alvarado et al., 2016;  
439 Yepes et al., 2016). Two destructive earthquakes ( $M_w \sim 7.0$ ), in the last 60 years (1955 and  
440 1987) (Hall, 2000; Yepes et al., 2016), occurred along the northern portion of this  
441 segment. Focal mechanism for the 1987,  $M_w$  7.0 (mainshock) and  $M_w$  5.8 (aftershock)  
442 show thrust and strike-slip respectively (Kawakatsu and Proaño, 1991). The strain rate  
443 tensor is also in agreement with a right-lateral transpressive regime for this segment.

444 The Pallatanga seismic source (zone 3) includes the Pallatanga fault itself and the  
445 continuously active Pisayambo seismic nest (Aguilar et al., 1996; Troncoso, 2008). The  
446 fault cuts diagonally the Inter-Andean-Valley across the Riobamba basin where it seems to  
447 divide into several segments (Baize et al., 2015). In its southwestern part, the Pallatanga  
448 fault is a right-lateral strike-slip fault (Winter et al., 1993), for which a 1300-3000 year-  
449 long recurrence time of  $M_w \sim 7.5$  earthquakes has been reported from a paleo-seismology  
450 study (Baize et al., 2015). The last earthquake occurred in 1797 and generated the highest  
451 intensities [magnitude 7.6 derived from intensities, XI MKS] reported in Ecuador (Egred,  
452 2000; Beauval et al., 2010). Focal mechanisms of small magnitude earthquakes show a  
453 combination of right-lateral and thrust motions. The northern part of the Pallatanga fault  
454 system (Pisayambo) shows highly recurrent seismicity (Segovia and Alvarado, 2009). In  
455 this area, the analysis of an  $M_w$  5.0 earthquake in 2010, combining InSAR, seismic and  
456 field observations, evidences a steeply dipping fault plane ( $> 50^\circ$ ) with right lateral  
457 displacement (Champenois et al., 2017). Compressional behavior with right-lateral  
458 component is indicated by the GPS derived strain rate tensor.

459 The southernmost segment of CCPP, the Puná seismic source (zone 4) is described  
460 as a strike-slip structure, based on geomorphic observations in the Puná Island (Dumont  
461 et al., 2005). Dumont et al. (2005) calculated a Holocene slip rate of 5.8 to 8 mm/yr which  
462 is consistent with the relative motion between the NAS and Inca Sliver (Nocquet et al.,  
463 2014). No large historical earthquakes have been reported for this segment. The FMs show  
464 dextral mechanisms on NE oriented planes, which are consistent with the expected fault  
465 direction and the predominant dextral components derived from the strain rate (Fig. 10).  
466 A small group of events including a  $M_w$  5.0 earthquake at the foot of the western Andes  
467 shows reverse motion with  $\sim$ EW shortening. This area behaves like a restraining bend  
468 linked to non-coplanar segments of the CCPP fault system, similarly to the New Madrid  
469 seismic zone (Marshak et al., 2003). In the Gulf of Guayaquil, the diversity of FMs solutions  
470 are the result of the complex tectonic environment. Strike-slip motion can be interpreted

471 as a result of activity in a transpressional structures like those observed in Puná Island  
472 (Deniaud et al., 1999; Fig. 10). The normal mechanism solutions are related to the drift of  
473 NAS, which induces a N-S tensional regime (Witt et al., 2006).

#### 4.2.2. The subandean domain

474 The Quaternary tectonics of the northern sub-Andean is not well known. The  
475 scarce seismicity and the lack of instrumentation, before 2009 (Alvarado et al., 2018), are  
476 responsible for the incomplete knowledge of the active tectonics in that zone. Toward the  
477 South, thanks to specific works carried out after the 1995 Macas earthquake (Mw 7.1), the  
478 tectonics of the Cutucú uplift is better understood.

479 The subandean domain is dominated by reverse faulting (Rivadeneira and Baby,  
480 2004). In northern Ecuador, the Napo uplift (zone 5) is considered to result from a sub-  
481 horizontal crustal decollement steepening close to the surface (Rivadeneira et al, 2004).  
482 Reverse FMs show variable fault plane azimuths (Fig. 10) which can be the expression of  
483 such type of structures. The strain rates are the lowest of the described zones, probably  
484 because most of the deformation is absorbed by the CCPP system and faults in the NAS.  
485 From the strain tensor, a dominant E-W shortening is expected for this area (Fig. 10).

486 The southeastern Cutucú seismic zone (zone 6) is the source of the 1995 Macas  
487 earthquake (Mw 7.0, GCMT); it is a complex system with almost parallel thrusts and  
488 decollements with a NNE trend (Bes de Berc, 2003). The complexity of the fault system  
489 could be an element explaining the diversity of the observed mechanisms (reverse and  
490 strike-slip, shown by both MECAVEL and GCMT solutions; see Fig. 8). However, we cannot  
491 exclude the possibility that some solutions (e.g. around latitude  $\sim 2^{\circ}\text{S}$  and longitude

492 ~77.6°W) are not accurately determined, due to the absence of stations east of the  
493 earthquakes. The strain rate is relatively low and shows shortening in a NW-SE direction  
494 (Fig. 10), which is consistent with the existence of the Cutucú Range and its NNE strike.

#### 495 **4.2.3. Western cordillera**

496 The El Angel fault (zone 8) is the southernmost expression of NNE trending  
497 structures that are clearly recognizable along the western slopes of the Cordillera Central  
498 in Colombia, defined as the Romeral fault system (París et al., 2000). Geomorphic  
499 lineaments have **right-lateral** strike-slip motion (Ego et al., 1995). In 1868, a segment  
500 attributed to this system ruptured twice with  $M_{ic}$  (magnitude based on intensity  
501 observations) of 6.6 and 7.2, respectively (Beauval et al., 2010). In the recent years  
502 analyzed here, seismicity concentrates close to the Cerro Negro-Chiles volcanic complex,  
503 where a magmatic intrusion likely started in the second semester of 2013 (Ebmeier et al.,  
504 2016). The main  $M_w$  5.6 earthquake, studied using satellite radar data (Ebmeier et al.,  
505 2016), shows a predominantly right-lateral slip with a slight reverse component, in  
506 agreement with the MECAVEL solution. The other FMs also show right-lateral strike-slip  
507 motion and E-W shortening, but no comparison can be done here with a GPS-derived  
508 strain tensor, due to the insufficient GPS coverage of the area (Fig. S1).

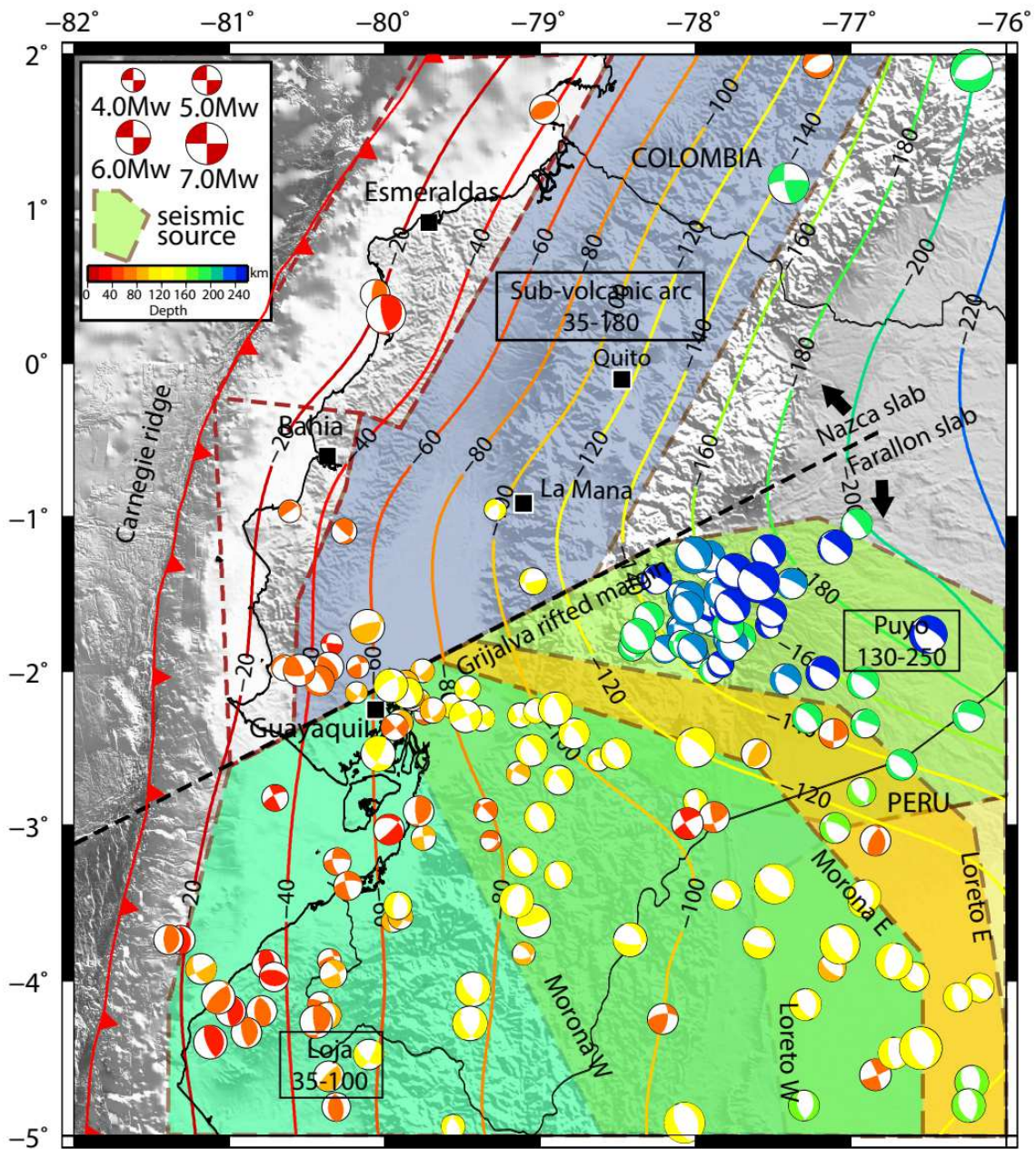
509 The Quito and Latacunga seismic sources (zone 9) are composed by blind reverse  
510 faults, folds and flexures at the surface, delimiting a possible block separated from the NAS  
511 (Alvarado et al., 2016). The Quito portion (N-S direction and ~60 km long) is a five sub-  
512 segments structure, which can rupture individually or simultaneously with magnitudes  
513 from 5.7 to 7.1 (Alvarado et al., 2014). The FMs in this section show ~N-S reverse planes  
514 which are consistent with the shortening predicted by the strain rates derived from GPS

515 velocities. Along the Latacunga segment, we only have one solution with a N-S nodal plane  
516 indicating EW shortening, in agreement with the proposed kinematic model from Lavenu  
517 et al. (1995) and Alvarado et al. (2016).

### 518 **4.3. Deep sources**

519 The **intermediate and** deep seismicity is related to the subduction of Nazca and  
520 Farallon slabs (Fig. 12). The Nazca slab, however, only hosts a weak and low magnitude  
521 seismicity in Ecuador. We could solve for two intermediate-depth FMs (~100 km), in the  
522 area of La Mana (Fig. 12), which both show a combination of normal and strike-slip  
523 mechanisms. The small number of events prevents us to properly describe the rupture  
524 characteristics of this seismic source.

525 The Farallon seismic sources located south of the extension of the Grijalva margin  
526 (Loja, Morona, Loreto and Puyo in Fig. 12) exhibit recurrent seismicity along the slab, from  
527 shallow (~35 km) to intermediate depths (~250 km). We generally observe that at least  
528 one of the nodal planes has a strike following the slab contour. At relatively shallow depths  
529 (between 40 and 90 km), from the Peru border to the Guayaquil area, the seismicity is  
530 mostly strike-slip (Fig. 12). The deeper seismicity is dominated by normal events, in  
531 agreement with the old deep part of the Farallon plate generating strong slab-pull forces  
532 (e.g. Chen et al., 2004). A highly active seismicity cluster is related to the el Puyo seismic  
533 nest, which spans over a wide range of depths from 130 to 250 km. Higher magnitude  
534 earthquakes appear to occur in the deeper portion of the nest, at depths around 200 km,  
535 as illustrated by the Mw 7.1 earthquake of August 2010. Another less dense and active  
536 normal-faulting cluster is located in the southeastern part of our study zone (Fig. 12), and  
537 shallower events (~120-160 km deep) are observed there.



538 **Fig. 12.** Joint CGMT and MECAVEL deep focal mechanisms (depth larger than 35 km). We follow the  
 539 denomination chosen by Yepes et al. (2016) for the name of the seismic sources zones and related  
 540 features. The Grijalva rifted margin (black dashed line) is believed to have a relevant role because it  
 541 separates two different slab domains with very different seismic activities (Yepes et al., 2016). The  
 542 focal mechanism depths and the iso-depths contours of the slab (Hayes et al., 2012) are color-coded  
 543 with the same scale, shown in the legend. The red thick line represents the trench.

## 544 **5. Conclusions**

545           We provide here a new catalog of earthquake focal mechanisms in Ecuador,  
546 obtained by waveform modeling. Our catalog includes 282 reliable solutions of source  
547 parameters for the period 2009-2015. This information includes the nodal plane angles as  
548 well as depth and moment magnitude determinations. Together with the GCMT solutions,  
549 our results provide new constraints on the interpretation of the tectonic processes at  
550 work in Ecuador. Combined with GPS-derived strain rates, these solutions put a better  
551 control on the deformation to be expected along and around the CCPP (Cosanga-Chingual-  
552 Pallatanga-Puná) fault system, which delimits the eastern boundary of the North Andean  
553 Sliver. In particular, the strike-slip character of the Puná fault, predicted by GPS strain  
554 rates and which was not fully recognized by the large magnitude GCMT mechanisms, now  
555 appears more clearly. At the Ecuador subduction zone, the focal mechanisms reflect the  
556 interseismic coupling derived from GPS: thrust interface mechanisms characterize the  
557 coupled interface in Northern Ecuador, while the low-to-moderate coupling in Central and  
558 Southern Ecuador results in variable fault plane orientations. This suggests that in case of  
559 low locking at the subduction interface, the stress field within the surrounding medium is  
560 poorly controlled by the plate motion and rather reflects heterogeneous deformation  
561 within the slab or the overriding crust.

## 562 Acknowledgments

563 We are grateful to the Secretaría Nacional de Educación Superior, Ciencia y  
564 Tecnología (SENESCYT, Ecuador) for funding the PhD scholarship of the first author of this  
565 study. This work has been supported by the Institut de Recherche pour le Développement  
566 of France (IRD) and the Instituto Geofísico, Escuela Politécnica Nacional (IG-EPN), Quito,  
567 Ecuador in the frame of the Joint International Laboratory 'Earthquakes and Volcanoes in  
568 the Northern Andes' (grant IRD 303759/00). Fundings from the Agence Nationale de la  
569 Recherche of France (grant ANR-07-BLAN-0143-01), SENESCYT (grant Fortalecimiento  
570 del Instituto Geofísico), SENPLADES (grant Generación de Capacidades para la Difusión de  
571 Alertas Tempranas), and collaboration with Instituto Geográfico Militar (IGM) are  
572 acknowledged. We thank all these partners for their strong support to the projects of  
573 geophysical instrumentation in Ecuador (national seismic and geodetic networks, and  
574 local ADN and JUAN projects). The installation and maintenance of the seismic and  
575 geodetic arrays would not have been possible without the help of numerous colleagues  
576 from the IRD and IG-EPN. The data from the OTAV station (IU network,  
577 <https://doi.org/10.7914/SN/IU>), retrieved at the IRIS Data Management Center, were  
578 used in this study. Numerical computations were partly performed on the S-CAPAD  
579 platform, IPGP, France. Comments and encouraging exchange of ideas with M. Segovia  
580 have contributed to enrich this study. Important remarks made during the review process,  
581 in particular by one of the two anonymous reviewers, were very helpful for this study. We  
582 finally thank the Editor (F. Audemard) for his careful rereading of the manuscript.

## 583 **Bibliography**

584           Aguilar, J., Chatelain, J.-L., Guillier, B., Yepes, H., 1996. The Pisayambo, Ecuador,  
585 Seismicity Nest: Towards the birth of a volcano? *Geodinámica Andina*, Troisième  
586 symposium international sur la Géodynamique Andine, Collection Colloques et Séminaires,  
587 ORSTOM édition, Paris, 126-129.

588           Aktug, B., Nocquet, J.-M., Cingöz, A. Parsons, B., Erkan, Y., England, P., 2009.  
589 Deformation of western Turkey from a combination of permanent and campaign GPS data:  
590 Limits to block-like behavior, *J. Geophys. Res.*, 114, B10404.  
591 <https://doi.org/10.1029/2008JB006000>

592           Alvarado, A., Audin, L., Nocquet, J.-M., Lagreulet, S., Segovia, M., Font, Y., Lamarque,  
593 G., Yepes, H., Mothes, P., Rolandone, F., Jarrin, P., Quidelleur, X., 2014. Active tectonics in  
594 Quito, Ecuador, assessed by geomorphological studies, GPS data, and crustal seismicity,  
595 *Tectonics*, 33, 67–83. <https://doi.org/10.1002/2012TC003224>

596           Alvarado, A., Audin, L., Nocquet, J.-M., Jaillard, E., Mothes, P., Jarrin, P., Segovia, M.,  
597 Rolandone, F., Cisneros, D., 2016. Partitioning of oblique convergence in the northern  
598 Andes subduction zone: Migration history and present-day boundary of the North Andean  
599 sliver in Ecuador, *Tectonics*, 35, 1048–1065. <https://doi.org/10.1002/2016TC004117>

600           Alvarado, A., Ruiz, M., Mothes, P., Yepes, H., Segovia, M., Vaca, M., Ramos, C.,  
601 Enríquez, W., Ponce, G., Jarrín, P., Aguilar, J., Acero, W., Vaca, S., Singaicho, J.C., Pacheco, D.,  
602 Córdova, A., 2018. Seismic, Volcanic, and Geodetic Networks in Ecuador: Building Capacity  
603 for Monitoring and Research, *Seismol. Res. Lett.*, 89, 432–439.  
604 <https://doi.org/10.1785/0220170229>

605 Audemard, F. A., 1993. Néotectonique, sismotectonique et aléa sismique du Nord-  
606 ouest du Vénézuéla (système de failles d'Oca-Ancón), PhD thesis, Université Montpellier II,  
607 Montpellier, France.

608 Audemard, F. E., & Audemard, F. A. (2002). Structure of the Mérida Andes,  
609 Venezuela: relations with the South America–Caribbean geodynamic interaction.  
610 *Tectonophysics*, 345(1-4), 1-26.

611 Avouac, J.-P., Meng, L., Wei, S., Wang, T., Ampuero, J.-P., 2015. Lower edge of locked  
612 Main Himalayan Thrust unzipped by the 2015 Gorkha earthquake, *Nat. Geosci.*, 8, 708-711,  
613 <https://doi.org/10.1038/ngeo2518>

614 Baize, S., Audin, L., Winter, T., Alvarado, A., Pilatasig, L., Taipe, M., Reyes, P.,  
615 Kauffman, P., Yepes, H., 2015. Paleoseismology and tectonic geomorphology of the  
616 Pallatanga fault (central Ecuador), a major structure of the South American crust,  
617 *Geomorphology*, 237, 14–28. <https://doi.org/10.1016/j.geomorph.2014.02.030>

618 Beauval, C., Yepes, H., Bakun, W., Egred, J., Alvarado, A., Singaicho, J.-C., 2010.  
619 Locations and magnitudes of historical earthquakes in the Sierra of Ecuador (1587-1996),  
620 *Geophys. J. Int.*, 181, 1613-1633. <https://doi.org/10.1111/j.1365-246X.2010.04569.x>

621 Beauval, C., Yepes, H., Palacios, P., Segovia, M., Alvarado, A., Font, Y., Aguilar, J.,  
622 Troncoso, L., Vaca, S., 2013. An earthquake catalog for seismic hazard assessment in  
623 Ecuador, *Bull. Seismol. Soc. Am.*, 103(2A), 773–786. <https://doi.org/10.1785/0120120270>

624 Beauval, C., Marinière, J., Yepes, H., Audin, L., Nocquet, J.-M., Alvarado, A., Baize, S.,  
625 Aguilar, J., Singaicho, J.-C., Jomard, H., 2018. A New Seismic Hazard Model for Ecuador,  
626 *Bull. Seismol. Soc. Am.*, 108(3A), 1443-1464. <https://doi.org/10.1785/0120170259>

627 Beck, S., Ruff, L., 1984. The rupture process of the great 1979 Colombia  
628 earthquake: Evidence for the asperity model, *J. Geophys. Res.*, 89, 9281–9291.  
629 <https://doi.org/10.1029/JB089iB11p09281>

630 Bes de Berc, S., 2003. Tectonique de chevauchement, surrection et incision  
631 fluviale (Exemple de la zone Subandine Equatorienne, haut bassin Amazonien), Thèse de  
632 doctorat, Université Toulouse III – Paul Sabatier.

633 Béthoux, N., Segovia, M., Alvarez, V., Collot, J.-Y., Charvis, P., Gailler, A., Monfret, T.,  
634 2011. Seismological study of the central Ecuadorian margin: Evidence of upper plate  
635 deformation, *J. South Am. Earth Sci.*, 31, 139–152.  
636 <https://doi.org/10.1016/j.jsames.2010.08.001>

637 Bishop, J.W., Lees, J.M., Ruiz, M.C., 2017. Receiver function stacks: initial steps for  
638 seismic imaging of Cotopaxi volcano, Ecuador. AGU Fall Meet. Abstr. 31.

639 Bonilla, L., Ruiz, M., Yepes, H., 1992. Evaluation of seismic hazard in Ecuador,  
640 Simposio Internacional sobre Prevención de Desastres Sísmicos, Mem. UNAM, Mexico,  
641 118–125.

642 Bouchon, M., 1981. A simple method to calculate Green's functions for elastic  
643 layered media, *Bull. Seismol. Soc. Am.*, 71(4), 959–971.

644 Calahorrano, A., 2005. Structure de la marge du Golfe de Guayaquil (Equateur) et  
645 propriétés physiques du chenal de subduction à partir de données de sismique marine  
646 réflexion et réfraction, Thèse de Doctorat, Université Pierre et Marie Curie (Paris VI).

647 Chambat, F., 1996. Figure de la Terre : Gravimétrie, régime de contraintes et  
648 vibrations, Thèse de Doctorat. Université Paris 7.

649 Champenois, J., Baize, S., Vallée, M., Jomard, H., Alvarado, A., Espin, P., Ekström, G.,  
650 Audin, L., 2017. Evidences of surface rupture associated with a low-magnitude (Mw 5.0)  
651 shallow earthquake in the Ecuadorian Andes, *J. Geophys. Res.*, 122, 8446–8458.  
652 <https://doi.org/10.1002/2017JB013928>

653 Chemenda, A., Lallemand, S., Bokun, A., 2000. Strain partitioning and interplate  
654 friction in oblique subduction zones: Constraints provided by experimental modeling, *J.*  
655 *Geophys. Res.*, 105(B3), 5567–5581. <https://doi.org/10.1029/1999JB900332>

656 Chen, P.-F., Bina, C. R., Okal, E. A., 2004. A global survey of stress orientations in  
657 subducting slabs as revealed by intermediate-depth earthquakes, *Geophys. J. Int.*, 159(2),  
658 721-733. <https://doi.org/10.1111/j.1365-246X.2004.02450.x>

659 Chlieh M., Mothes, P., Nocquet, J.-M., Jarrin, P., Charvis, P., Cisneros, D., Font, Y.,  
660 Collot, J.-Y., Villegas, J.-C., Rolandone, F., Vallée, M., Regnier, M., Segovia, M., Martin, X.,  
661 Yepes, H., 2014. Distribution of discrete seismic asperities and aseismic slip along the  
662 Ecuadorian megathrust, *Earth Planet. Sci. Lett.*, 400, 292-301.  
663 <https://doi.org/10.1016/j.epsl.2014.05.027>

664 Collot J.-Y., Michaud, F., Alvarado, A., Marcaillou, B., Sosson, M., Ratzov, G., Migeon,  
665 S., Calahorrano, A., Pazmiño, A., 2009. Visión general de la morfología submarina del  
666 margen convergente de Ecuador-Sur de Colombia: implicaciones sobre la transferencia de  
667 masa y la edad de la subducción de la Cordillera de Carnegie, *Geología y Geofísica Marina y*  
668 *Terrestre. Ecuador. Spec. Pub. INOCAR-IRD*, 47-74.

669 Collot, J.-Y., Sanclemente, E., Nocquet, J.-M., Leprêtre, A., Ribodetti, A., Jarrin, P.,  
670 Chlieh, M., Graindorge, D., Charvis, P., 2017. Subducted oceanic relief locks the shallow  
671 megathrust in central Ecuador, *J. Geophys. Res.*, 122, 3286–3305.  
672 <https://doi.org/10.1002/2016JB013849>

673 Delouis, B., 2014. FMNEAR: Determination of focal mechanism and first estimate of  
674 rupture directivity using near-source records and a linear distribution of point sources,  
675 Bull. Seismol. Soc. Am., 104, 1479–1500. <https://doi.org/10.1785/0120130151>

676 Deniaud, Y., Baby, P., Basile, C., Ordoñez, M., Montenegro, G., Mascle, G., 1999.  
677 Opening and tectonic and sedimentary evolution of the Gulf of Guayaquil: Neogene and  
678 Quaternary fore-arc basin of the south Ecuadorian Andes, C. R. Acad. Sci. Paris, 328, 181–  
679 187.

680 Dumont, J.-F., Santana, E., Vilema, W., Pedoja, K., Ordóñez, M., Cruz, M., Jiménez, N.  
681 Zambrano, I., 2005. Morphological and microtectonic analysis of Quaternary deformation  
682 from Puná and Santa Clara Islands, Gulf of Guayaquil, Ecuador (South America),  
683 Tectonophysics, 399(1-4), 331–350. <https://doi.org/10.1016/j.tecto.2004.12.029>

684 Durand, P., Massinon, B., Menechal, Y., Troiville, C., 1987. Etude sismique du site de  
685 Mica-Tambo (Equateur), Commissariat à l'Energie Atomique, Laboratoire de Géophysique,  
686 Rapport No.1.

687 Dziewonski, A., Chou, T., Woodhouse, J., 1981. Determination of earthquake source  
688 parameters from waveform data for studies of global and regional seismicity, J. Geophys.  
689 Res., 86, 2825–2852. <https://doi.org/10.1029/JB086iB04p02825>

690 Ebmeier, S., Elliott, J., Nocquet, J.-M., Biggs, J., Mothes, P., Jarrín, P., Yépez, M.,  
691 Aguaiza, S., Lundgren, P., Samsonov, S., 2016. Shallow earthquake inhibits unrest near  
692 Chiles–Cerro Negro volcanoes, Ecuador–Colombian border, Earth Planet. Sci Lett., 450,  
693 283-291. <https://doi.org/10.1016/j.epsl.2016.06.046>

694 Ego, F., Sébrier, M., Yepes, H., 1995. Is the Cauca-Patia and Romeral fault system left  
695 or right lateral? Geophys. Res. Lett., 22, 33–36. <https://doi.org/10.1029/94GL02837>

696 Ego, F., Sébrier, M., Lavenu, A., Yepes, H., Egüez, A., 1996. Quaternary state of stress  
697 in the northern Andes and the restraining bend model for the Ecuadorian Andes,  
698 *Tectonophysics*, 259(1), 101–116. [https://doi.org/10.1016/0040-1951\(95\)00075-5](https://doi.org/10.1016/0040-1951(95)00075-5)

699 Egred, J., 2000. *El Terremoto de Riobamba*, Ed. Abya Yala, Quito.

700 Egüez, A., Alvarado, A., Yepes, H., Machette, M., Costa, C., Dart, R., 2003. Database  
701 and Map of Quaternary faults and folds of Ecuador and its offshore regions. U.S. Geol.  
702 Survey Open File Report, 03-289, 1–77.

703 Ekström, G., Nettles, M., Dziewonski, A., 2012. The global CMT project 2004–2010:  
704 centroid-moment tensors for 13,017 earthquakes, *Phys. Earth. Planet. Inter.*, 200(201), 1–  
705 9. <https://doi.org/10.1016/j.pepi.2012.04.002>

706 Font, Y., Segovia, M., Vaca, S., Theunissen, T., 2013. Seismicity pattern along the  
707 Ecuadorian subduction zone: new constraints from earthquake location in a 3D a priori  
708 velocity model, *Geophys. J. Int.*, 193, 263–286. <https://doi.org/10.1093/gji/ggs083>

709 Grandin, R., Vallée, M., Lacassin, R., 2017. Rupture process of the Oklahoma Mw 5.7  
710 Pawnee earthquake from Sentinel-1 InSAR and seismological data, *Seismol. Res. Lett.*, 88,  
711 994-1004. <https://doi.org/10.1785/0220160226>

712 Freymueller, J., Kellogg, J., Vega, V., 1993. Plate Motions in the north Andean region,  
713 *J. Geophys. Res.*, 98, 21853–21863. <https://doi.org/10.1029/93jb00520>

714 Hall, M., 2000. Los terremotos del Ecuador del 5 de marzo de 1987 deslizamientos  
715 y sus efectos socioeconómicos, Colección de Estudios de Geografía, Volumen 9,  
716 Corporación Editora Nacional, Quito, Ecuador.

717 Hayes, G., Wald, D., Johnson, R., 2012. Slab1.0: a three-dimensional model of global  
718 subduction zone geometries, *J. Geophys. Res.*, 117, B01302.  
719 <https://doi.org/10.1029/2011JB008524>

720 Jarrin, P., 2015. Modelamiento de datos GPS aplicado al estudio de la subducción en  
721 el Ecuador. Reporte de Master. Escuela Politécnica Nacional, Quito-Ecuador.

722 Kanamori, H., McNally, K., 1982. Variable rupture mode of the subduction zone  
723 along the Ecuador-Colombia coast, *Bull. Seismol. Soc. Am.*, 72, 1241–1253.

724 Kawakatsu, H., Proaño, G., 1991. Focal Mechanisms of the March 6, 1987 Ecuador  
725 Earthquakes, *J. Phys. Earth.* 39, 589-597. <https://doi.org/10.4294/jpe1952.39.589>

726 Kelleher, J., 1972. Rupture zones of large South American earthquakes and some  
727 predictions, *J. Geophys. Res.*, 77, 2087–2103. <https://doi.org/10.1029/JB077i011p02087>

728 Kellogg, J., Bonini, W., 1982. Subduction of the Caribbean Plate and Basement,  
729 uplifts in the overriding South American Plate, *Tectonics*, 1(3), 251-276.  
730 <https://doi.org/10.1029/TC001i003p00251>

731 Kellogg, J., Ogujiofor, I., Kansaka, D., 1985. Cenozoic tectonics of the Panama and  
732 North Andes blocks. *Memorias Congreso Latinoamericano de Geología*, 6, 34-49.

733 Kendrick, E., Bevis, M., Smalley, R., Brooks, B., Vargas, R., Lauría, E., Fortes, L., 2003.  
734 The Nazca-South America Euler vector and its rate of change, *J. S. Am. Earth Sci.*, 16, 125–  
735 131. [https://doi.org/10.1016/S0895-9811\(03\)00028-2](https://doi.org/10.1016/S0895-9811(03)00028-2)

736 Lavenu, A., Winter, T., Dávila, F., 1995. A Pliocene-Quaternary compressional basin  
737 in the Interandean Depression Central Ecuador, *Geophys. J. Int.*, 121, 279–300.  
738 <https://doi.org/10.1111/j.1365-246X.1995.tb03527.x>

739 Lonsdale, P., 2005. Creation of the Cocos and Nazca plates by fission of the Farallon  
740 plate, *Tectonophysics*, 404, 237-264. <https://doi.org/10.1016/j.tecto.2005.05.011>

741 López, E., 2005. 132 años de historia del Observatorio Astronómico de Quito,  
742 Observatorio Astronómico Nacional, Escuela Politécnica Nacional.

743 Marshak, S., Nelson, W., McBride, J., 2003. Phanerozoic strike-slip faulting in the  
744 continental interior platform of the United States: Examples from the Laramide Orogen,  
745 midcontinent, and Ancestral Rocky Mountains, *Geological Society Special Publication*, 210,  
746 159-184. <https://doi.org/10.1144/GSL.SP.2003.210.01.10>

747 McCaffrey, R., 1992. Oblique plate convergence, slip vectors, and forearc  
748 deformation, *J. Geophys. Res.*, 97(B6), 8905–8915. <https://doi.org/10.1029/92JB00483>

749 McNutt, S., 2005. Volcano seismology, *Annu. Rev. Earth Planet. Sci.*, 33, 461 – 491.

750 Mendoza, C., Dewey, J., 1984. Seismicity associated with the great Colombia-  
751 Ecuador earthquakes of 1942, 1958, and 1979: Implications for barrier models of  
752 earthquake rupture, *Bull. Seismol. Soc. Am.*, 74(2), 577–593.

753 Mercier de Lépinay, B., Deschamps, A., Klingelhoefer, F., Mazabraud, Y., Delouis, B.,  
754 Clouard, V., Hello, Y., Crozon, J., Marcaillou, B., Graindorge, D., Vallée, M., Perrot, J., Bouin,  
755 M.-P., Saurel, J.-M., Charvis, P., St-Louis, M., 2011. The 2010 Haiti earthquake: A complex  
756 fault pattern constrained by seismologic and tectonic observations, *Geophys. Res. Lett.*, 38,  
757 L22305. <https://doi.org/10.1029/2011GL049799>

758 Michaud, F., Collot, J.-Y., Alvarado, A., López, E., and the scientific and technical  
759 team of INOCAR, 2006. *Batimetría y Relieve Continental*, publication IOA-CVM-02-Post,  
760 Inst. Oceanogr. de la Armada del Ecuador, Guayaquil.

761 Minson, S., Dreger, D., Burgmann, R., Kanamori, H., Larson, K., 2007. Seismically and  
762 geodetically determined nondouble-couple source mechanisms from the 2000 Miyakejima  
763 volcanic earthquake swarm, *J. Geophys. Res.*, 112, 10308.  
764 <https://doi.org/10.1029/2006JB004847>

765 Mora-Páez, H., Kellogg, J., Freymueller, J., Mencin, D., Fernandes, R., Diederix, H.,  
766 LaFemina, P., Cardona-Piedrahita, L., Lizarazo, S., Peláez-Gaviria, J.-R., Díaz-Mila, F.,  
767 Bohórquez-Orozco, O., Giraldo-Londoño, L., Corchuelo-Cuervo, Y., 2018. Crustal  
768 deformation in the northern Andes – A new GPS velocity field, *J. South Am. Earth Sci.*, 89,  
769 76–91. <https://doi.org/10.1016/j.jsames.2018.11.002>

770 Mothes, P., Nocquet, J.-M., Jarrin, P., 2013. Continuous GPS network operating  
771 throughout Ecuador. *Eos. Transactions AGU*, 94 (26), 229-231.  
772 <https://doi.org/10.1002/2013E0260002>

773 Mothes, P., Rolandone, F., Nocquet, J.-M., Jarrin, P., Alvarado, A., Ruiz, M., Cisneros,  
774 D., Mora-Páez, H., Segovia, M., 2018. Monitoring the earthquake cycle in the northern  
775 Andes from the Ecuadorian cGPS network. *Seismol. Res. Lett.*, 89, 534-541.  
776 <https://doi.org/10.1785/0220170243>

777 Nocquet, J.-M., Yepes, H., Vallée, M., Mothes, P., Regnier, M., Segovia, S., Font, Y.,  
778 Vaca, S., Béthoux, N., Ramos, C., 2010. The ADN project: an integrated seismic monitoring  
779 of the northern Ecuadorian subduction, EGU General Assembly 2010, Vienna, Austria,  
780 9913.

781 Nocquet, J.-M., Villegas, J.-C., Chlieh, M., Mothes, P., Rolandone, F., Jarrin, P.,  
782 Cisneros, D., Alvarado, A., Audin, L., Bondoux, F., Martin, X., Font, Y., Régnier, M., Vallée, M.,  
783 Tran, T., Beauval, C., Maguiña, J., Martinez, W., Tavera, H., Yepes, H., 2014. Motion of  
784 continental slivers and creeping subduction in the northern Andes, *Nat. Geosci.*, 7, 287–  
785 291. <https://doi.org/10.1038/ngeo2099>

786 Nocquet, J-M., Jarrin, P., Vallée, M., Mothes, P., Grandin, R., Rolandone, F., Delouis, B.,  
787 Yepes, H., Font, Y., Fuentes, D., Régnier, M., Laurendeau, A., Cisneros, D., Hernandez, S.,  
788 Sladen, A., Singaicho, J.-C., Mora, H., Gomez, J., Montes, L., Charvis, P., 2017. Supercycle at  
789 the Ecuadorian subduction zone revealed after the 2016 Pedernales earthquake, Nat.  
790 Geosci., 10, 145-149. <https://doi.org/10.1038/NGEO2864>

791 París, G., Machette, M., Dart, R., Haller, K., 2000. Map and database of Quaternary  
792 faults and folds in Colombia and its offshore regions, U.S. Geol. Survey Open File Report,  
793 00-0284.

794 Pennington, W., 1981. Subduction of the Eastern Panama Basin and  
795 seismotectonics of northwestern South America, J. Geophys. Res., 86.  
796 <https://doi.org/10.1029/JB086iB11p10753>

797 Poveda, E., Monsalve, G., Vargas, C., 2015. Receiver functions and crustal structure  
798 of the northwestern Andean region, Colombia, J. Geophys. Res. Solid Earth, 120, 2408–  
799 2425. <https://doi.org/10.1002/2014JB011304>

800 Rivadeneira, M., Baby, P., 2004. Características geológicas de los principales  
801 campos petroleros de Petroproducción, Travaux de l'Institut Français d'Etudes Andines,  
802 144.

803 Rivadeneira, M., Baby, P., Barragán, R., 2004. La Cuenca Oriente: geología y  
804 petróleo, Travaux de l'Institut Français d'Etudes Andines, 144.

805 Robalino, F., 1977. Espesor de la corteza en Quito mediante el análisis del espectro  
806 de las ondas longitudinales P de período largo, Instituto Panamericano de Geografía e  
807 Historia, XI Asamblea General, Sección Nacional del Ecuador. Quito-Ecuador.

808 Rolandone, F., Nocquet, J.-M., Mothes, P.A., Jarrin, P., Vallée, M., Cubas, N.,  
809 Hernandez, S., Plain, M., Vaca, S., Font, Y., 2018. Areas prone to slow slip events impede  
810 earthquake rupture propagation and promote afterslip, *Sci. Adv.*, 4, eaa06596.  
811 <https://doi.org/10.1126/sciadv.aao6596>

812 Sambridge, M., 1999. Geophysical inversion with a neighbourhood algorithm- I.  
813 Searching a parameter space, *Geophys. J. Int.*, 138, 479-494.  
814 <https://doi.org/10.1046/j.1365-246X.1999.00876.x>

815 Segovia, M., Pacheco, J., Shapiro, N., Yepes, H., Guillier, B., Ruiz, M., Calahorrano, A.,  
816 Andrade, D., Egred, J., 1999. The Agust 4, 1998, Bahía Earthquake (Mw=7.1): Rupture  
817 mechanism and comments on the potencial seismic activity, Fourth ISAG, Germany, 673-  
818 677.

819 Segovia, M., Alvarado, A., 2009. Breve análisis de la sismicidad y del campo de  
820 esfuerzos en el Ecuador, *Geología y Geofísica Marina y Terrestre, Ecuador. Spec. Pub.*  
821 *INOCAR-IRD*, 131-149.

822 Segovia Reyes, M., 2016. Imagerie microsismique d'une asperité sismologique dans  
823 la zone de subduction Équatorienne. Thèse de doctorat, Université Nice-Sophia Antipolis.

824 Segovia, M., Font, Y., Régnier, M., Charvis, P., Galve, A., Nocquet, J.-M., et al.,  
825 2018. Seismicity distribution near a subducting seamount in the Central Ecuadorian  
826 subduction zone, space-time relation to a slow-slip event. *Tectonics*, 37, 2106-  
827 2123. <https://doi.org/10.1029/2017TC004771>

828 Shuler, A., Ekström, G. 2009. Anomalous earthquakes associated with Nyiragongo  
829 Volcano: Observations and potential mechanisms, *J. Volc. Geotherm. Res.*, 181, 219-230.  
830 <https://doi.org/10.1016/j.jvolgeores.2009.01.011>

831 Soulas, J.-P., Egüez, A., Yepes, H., Pérez, V-H., 1991. Tectónica activa y riesgo sísmico  
832 en los Andes Ecuatorianos y en el extremo Sur de Colombia, Bol. Geol. Ecuatoriano, 2(1),  
833 3-11.

834 Swenson, J., Beck, S., 1996. Historical 1942 Ecuador and 1942 Peru subduction  
835 earthquakes and earthquake cycles along Colombia, Ecuador and Peru subduction  
836 segments, Pure Appl. Geophys., 146(1), 67-101.

837 Taboada, C., Dimaté, C., Fuenzalida, A., 1998. Sismotectónica de Colombia:  
838 deformación continental activa y subducción, Física de la Tierra, 10, 111-147.

839 Tibaldi, A., Rovida, A., Corazzato, C., 2007. Late Quaternary kinematics, slip-rate  
840 and segmentation of a major Cordillera-parallel transcurrent fault: The Cayambe-  
841 Afiladores-Sibundoy system, NW South America, J. Struct. Geol., 29(4), 664-680.  
842 <https://doi.org/10.1016/j.jsg.2006.11.008>

843 **Trenkamp, R., Kellogg, J., Freymueller, J., Mora, H., 2002. Wide plate margin**  
844 **deformation, southern Central America and northwestern South America, CASA GPS**  
845 **observations, J. South Am. Earth Sci., 15, 157-171.**

846 Troncoso, L., 2008. Estudio sismológico del nido de Pisayambo, Reporte de Master.  
847 Escuela Politécnica Nacional, Quito-Ecuador.

848 Vaca, S., 2006. Elaboración de un modelo 3D de velocidades sísmicas de ondas para  
849 el Ecuador y relocalización de eventos sísmicos entre 1995 y 2005, Tesis de ingeniería,  
850 Facultad de Geología, Escuela Politécnica Nacional, Quito-Ecuador, 63-66.

851 Vaca, S., Régnier, M., Bethoux, N., Alvarez, V., Pontoise, B., 2009. Sismicidad de la  
852 región de Manta: Enjambre sísmico de Manta-2005, Geología y Geofísica Marina y  
853 Terrestre, Ecuador. Spec. Pub. INOCAR-IRD, 155-166.

854 Vaca, S., Vallée, M., Nocquet, J.-M., Battaglia J., Regnier, M., 2018. Recurrent Slow  
855 Slip Events as a barrier to the northward rupture propagation of the 2016 Pedernales  
856 earthquake (Central Ecuador), *Tectonophysics*, 724-725, 80-92.  
857 <https://doi.org/10.1016/j.tecto.2017.12.012>

858 [dataset] Vaca, S., Vallée, M., Nocquet, J.-M., Alvarado, A., Seismic source parameters  
859 of the 282 Ecuador earthquakes (2009-2015) determined by the MECAVEL method,  
860 Mendeley data, 2019.

861 Vallée M, Nocquet, J.-M., Battaglia, J., Font, Y., Segovia, M., Régnier, M., Mothes, P.,  
862 Jarrin, P., Cisneros, D., Vaca, S., Yepes, H., Martin, X., Béthoux, N., Chlieh, M., 2013. Intense  
863 interfece seismiscity triggered by a shallow slow slip event in the Central Ecuador  
864 subduction zone, *J. Geophys. Res.*, 118, 1-17. <https://doi.org/10.1002/jgrb.50216>

865 Villegas-Lanza, J.-C., Chlieh, M., Cavalié, O., Tavera, H., Baby, P., Chire-Chira, J.,  
866 Nocquet, J.-M., 2016. Active tectonics of Peru: Heterogeneous interseismic coupling along  
867 the Nazca megathrust, rigid motion of the Peruvian Sliver, and Subandean shortening  
868 accommodation, *J. Geophys. Res.*, 121, 7371-7394.  
869 <https://doi.org/10.1002/2016JB013080>

870 Winter, T., Avouac, J.-P., Lavenu, A., 1993. Late Quaternary kinematics of the  
871 Pallatanga strike-slip fault (Central Ecuador) from topographic measurements of  
872 displaced morphological features, *Geophys. J. Int.*, 115, 905-920.  
873 <https://doi.org/10.1111/j.1365-246X.1993.tb01500.x>

874 Witt, C., Bourgois, J., Michaud, F., Ordoñez, M., Jiménez, N., Sosson, M., 2006.  
875 Development of the Gulf of Guayaquil (Ecuador) during the Quaternary as an effect of the  
876 North Andean Block tectonic escape, *Tectonics*, 25, TC3017.  
877 <https://doi.org/10.1029/2004TC001723>

878 Ye, L., Kanamori, H., Avouac, J.-P., Li, L., Cheung, K., Lay, T., 2016. The 16 April 2016,  
879 Mw 7.8 (MS 7.5) Ecuador earthquake: A quasi-repeat of the 1942 MS 7.5 earthquake and  
880 partial re-rupture of the 1906 MS 8.6 Colombia–Ecuador earthquake, *Earth Planet. Sci.*  
881 *Lett.*, 454, 248-258. <https://doi.org/10.1016/j.epsl.2016.09.006>

882 Yepes, H., 1982. Estudio de la actividad microsísmica en el Valle Interandino entre  
883 las latitudes 0.00° y 1.00° S, Tesis Ing. Geólogo, Escuela Politécnica Nacional. Quito, 1-98.

884 Yepes, H., Audin, L., Alvarado, A., Beauval, C., Aguilar, J., Font, Y., Cotton, F., 2016. A  
885 new view for the geodynamics of Ecuador: Implication in seismogenic source definition  
886 and seismic hazard assessment, *Tectonics*, 35, 1249–1279.  
887 <https://doi.org/10.1002/2015TC003941>

888 Yoshimoto, M., Kumagai, H., Acero, W., Ponce, G., Vásconez, F., Arrais, S., Ruiz, M.,  
889 Alvarado, A., Pedraza-García, P., Dionicio, V., Chamorro, O., Maeda, Y., Nakano, M., 2017.  
890 Depth-dependent rupture mode along the Ecuador-Colombia subduction zone, *Geophys.*  
891 *Res. Lett.*, 44, 2203–2210. <https://doi.org/10.1002/2016GL071929>

892 Zahradník, J., Janský, J., Plicka, V., 2008. Detailed waveform inversion for moment  
893 tensors of  $M \sim 4$  events; examples from the Corinth Gulf, Greece, *Bull. Seismol. Soc. Am.*, 98,  
894 2756-2771. <http://doi.org/10.1785/0120080124>

895